Generalized theoretical framework for spatial attenuation rates of gravity waves in a stepwise-stratified fluid system with multiple layers of arbitrary depths

L. Suswanth and Girish Kumar Rajan [*]
WAVES Laboratory, Department of Mechanical Engineering, Indian Institute of Technology Tirupati, AP 517619, India

(Received 2 January 2025; accepted 31 March 2025; published 19 May 2025)

This study presents a theoretical model for gravity wave attenuation in a multilayered fluid system comprising fluidized mud, water, an interfacial fluid layer (typically enriched with surface-active compounds including oil), and air, which closely mimics the atmosphere-ocean configuration. A rigorous mathematical analysis initiated from the boundary value problem yields the dispersion relation, which is then solved numerically to obtain the complex-valued wave number, whose imaginary part is the spatial attenuation rate. Parametric studies are conducted to investigate how the attenuation rate responds to changes in wave frequencies, fluid and interfacial properties, and layer depths. Results obtained are compared with published experimental data in select cases, showing good agreement. In addition, the model is applied to reduced systems by setting the densities or depths of select layers to zero. For a water-mud system, maximum attenuation rates occur when the mud layer's depth is comparable to the wavelength and exceeds the boundary layer thickness by 100%–200%. Similarly, in an oil-water-mud system, maximum attenuation rates are obtained when the mud layer's depth exceeds the boundary layer thickness by 10%. Further analysis highlights the significance of air dynamics through the ratio, α, defined as the attenuation rate in an air-oil-water-mud system relative to that in a corresponding vacuum-oil-water-mud system. Results reveal that $\alpha \gg 1$ for low-frequency waves in deep water systems, with values reaching up to 10^3 in specific cases. Such high values underscore the critical role of air dynamics in predicting attenuation rates accurately. Moreover, in an air-oil-water-mud system, the maximum value of α and the corresponding frequency at which it occurs exhibit power-law dependencies on water layer depth (d_2), scaling as $d_2^{2/3}$ and $d_2^{-1/2}$, respectively. It is inferred that maximum attenuation rates are linked to strong velocity gradients in the fluid layers; they may also be understood by analyzing variations in the group velocity and the penetration depth, which is related to the rotational part of the velocity field.

DOI: 10.1103/PhysRevFluids.10.054802

I. INTRODUCTION

Conditions at the atmosphere-ocean boundary regulate the dynamic coupling between air and water, so it is important to study them extensively to understand global climate patterns and extreme weather events. Surface gravity waves (SGWs) play a key role in this coupling by influencing transport phenomena across the boundary (see [1–3]). In fact, the effect of SGW attenuation on the modification of air-sea fluxes has been well documented [4–6]. Furthermore, investigation of

[*]Contact author: gkrpsu@gmail.com

SGW attenuation is critical for several applications, including weather prediction, coastal erosion, ocean mixing, and human activities such as ship routing. Attempting to build on existing research, this study conducts an extensive investigation of SGW attenuation in a multilayered fluid system, considering several factors that affect it.

A. Relevant mechanisms of SGW attenuation

The attenuation of SGW is affected by various mechanisms; here we focus on those pertinent to our study.

(1) *Boundary layer effects due to finite depth.* Several models that predict the attenuation rates of SGWs such as ocean swell consider an infinitely deep water layer (see [6–8], for example). This is justified when the depth of water layer is substantially greater than the wavelength, which effectively renders the bottom undetectable to these waves. In contrast, nearshore wave propagation—where the depth of water layer is comparable to or less than the wavelength—requires consideration of viscous effects at the ocean floor. Studies have demonstrated that bottom friction substantially enhances SGW attenuation in finite-depth waters (see [9–12]). When the depth of water layer is below a threshold value, rotational motions within the bottom boundary layer contribute to the dissipation of surface waves. In addition to affecting dissipation, wave-bottom interactions have significant consequences for coastal engineering due to their influence on design considerations, structural lifespan, estimation of turbidity levels, and modeling sediment transport.

(2) *Internal friction in a fluid-like mud layer.* Conventional models which account for bottom friction assume an impermeable seafloor. A seminal work by Dalrymple and Liu [13] challenged this assumption, analyzing the impact of a muddy seabed on SGW attenuation. Their innovative work sparked subsequent studies on related topics (see [13–21]). A realistic representation of the atmosphere-ocean system includes a finitely deep water layer overlying a thick, fluid-like mud layer. Interestingly, the fluidization of marine mud is often facilitated by wave activity (see [22,23]). In fact, the report of Elgar and Raubenheimer [19] reveals the presence of seafloor mud with a yogurt-like consistency, validating the assumption of a dense fluid layer interposed between the water layer and rocky seabed. Mud layers in marine environments are typically characterized by thicknesses of a few centimeters to a few meters, and bulk friction in such layers significantly contributes to the attenuation of SGWs (e.g., [14,20,24–26]).

(3) *Dynamics of an interfacial fluid layer.* The ocean's skin, a thin interfacial fluid layer separating air from bulk water, comprises a complex mixture of oil from spillage, emulsions, phytoplankton, zooplankton, biogenic films, crud, and various natural and anthropogenic constituents that define the sea surface microlayer (see [27–29]). Analyses of synthetic aperture radar images have revealed that such a complex mixture can affect SGW attenuation by modifying the sea-surface roughness (see [30,31]). Due to its distinct dynamics, the interfacial fluid layer, with thickness ranging from a few micrometers to millimeters, has a significant impact on wave attenuation, which necessitates its inclusion in models for accurate predictions (see [29,32]). The concept of wave attenuation due to an interfacial fluid layer has been intuitively applied for centuries. Notably, the ancient practice of pouring oil on turbulent waters to calm waves, first documented by Pliny the Elder, has been a trusted tactic for fishermen and voyagers seeking to quieten violent seas (see [33–36] and references therein).

(4) *Air dynamics.* Multiple studies (see [6,7,37]) highlight the significant role of air in attenuating swell waves. The effects of air are particularly pronounced for low-frequency waves, as models incorporating air dynamics predict substantially higher attenuation rates compared to those neglecting them. Furthermore, the kinematic viscosity of water is approximately an order of magnitude lower than that of air, despite water's density being three orders of magnitude greater, underscoring the importance of considering air dynamics in wave dissipation models, especially for long waves (see [6]).

(5) *Marangoni effect due to surfactants.* Thicknesses of surfactant monolayers formed at the air-seawater interface due to the deposition of marine by-products and terrestrial runoff are on

the order of 1 nm (see [38–41]). The dynamics of these monolayers introduce an additional wave attenuation mechanism (see [11,32,33,38,42–52] and references therein). The straining of a surfactant-contaminated interface leads to gradients in concentration caused due to surfactant molecules accumulating at crests and dispersing at troughs. These in turn induce corresponding gradients in interfacial tension, leading to the generation of Marangoni waves, which eventually drain energy from SGW.

There are several other mechanisms contributing to the loss of SGW energy, including turbulent mixing, wave breaking, white capping, and nonlinear interactions. Although important, these mechanisms are outside the scope of this study. For a comprehensive overview of energy dissipation mechanisms in SGW such as swell, see [5,6,8,53–58]. In Sec. I B we summarize existing research on wave attenuation models which have accounted for some of the factors discussed above.

B. A summary of existing models on wave attenuation

In his initial investigation of oscillatory motion in fluids, Stokes neglected wave dissipation [59,60]. Later, Sir Horace Lamb presented the fundamental theory of wave hydrodynamics in his book, investigating the attenuation of gravity waves propagating on the surface of an infinitely deep water layer, assuming it to be (i) clean and (ii) covered with a surfactant monolayer [61]. In our opinion, an early breakthrough in this field was made by Harrison [62], who generalized Lamb's theory by investigating the attenuation of gravity waves at a two-fluid interface. Since then, numerous studies on various aspects of wave attenuation have been published.

Contributions on SGW attenuation in one-fluid systems cover both experimental and theoretical aspects, exploring the effects of clean and surfactant-contaminated surfaces, and of finite depth (see [9,11,12,33,38,42–45,47–49,61,63–108]). With fewer variables to consider, single-fluid systems allow for a mathematically tractable framework. Typically, the dynamics of air are neglected in single-fluid models based on the argument that its density is three orders of magnitude lower than that of water. In reality, the atmosphere-ocean system is more complex than a single-fluid system, featuring muddy layers close to the sea floor and thick contaminant layers (created by oil spills and pollutants) which separate air from bulk water. To ensure greater consistency with the atmosphere-ocean system, researchers have generalized single-fluid models, leading to the development of two-fluid models for wave attenuation in systems with air-water, oil-water, and water-mud pairs (see the works of [6,10–17,26,32,37,51,62,83,89,100,109–144]). In order to show wider application, some studies have moved beyond the conventional air-water focus, incorporating diverse combinations such as kerosene and water (for instance, see [10]). Results from these investigations emphasize the importance of understanding fluid interactions in a variety of systems, with the atmosphere-ocean system remaining a widely considered application.

Although two-fluid models are better than one-fluid models in representing the atmosphere-ocean system, they fail to depict it completely. This drawback motivated the development of three-fluid models, specifically focusing on wave attenuation in air-oil-water and air-water-mud configurations. Despite the need for better predictions, research on wave attenuation in three-fluid systems remains scarce, with only a few exceptions (see [7,145,146]). Table I provides a systematic categorization of existing studies, compiled from an exhaustive review of relevant literature. A notable gap is revealed: no model integrates all crucial factors described in Sec. I A. To bridge this gap, we attempt to develop a generalized model to predict wave attenuation rates in this study. In Sec. I C, we elaborate on the key features and limitations of our proposed model.

C. Details of the present study

Motivated by the need for an inclusive framework, we investigate wave attenuation in a multi-layered fluid configuration (see Fig. 1) depicting the atmosphere-ocean system. This configuration consists of four distinct immiscible fluid layers: layer 1 (a finitely thick viscous mud layer), layer 2 (a finitely thick water layer), layer 3 (a finitely thick oil layer), and layer 4 (an infinitely deep air

TABLE I. Summary of studies on wave attenuation.

No.	Air (layer 4 in Fig. 1)	Oil (layer 3 in Fig. 1)	Water (layer 2 in Fig. 1)	Mud (layer 1 in Fig. 1)	Interfacial elasticity	Type	References
One-fluid models							
1	No	No	Yes, infinitely deep	No	No	Analytic	[61,63,64]
						Semianalytic	[65]
2	No	No	Yes, finitely deep	No	No	Analytic	[66–69]
						Experimental	[68–70]
3	No	No	Yes, infinitely deep	No	Yes	Analytic	[38,42,44,48,61,63,71–74]
						Experimental	[33,74,75]
						Semianalytic	[76]
4	No	No	Yes, finitely deep	No	Yes	Analytic	[9,43–45,47,49,77–86,88,102,103]
						Experimental	[9,11,12,49,78,84,87–107]
						Semianalytic	[108]
Two-fluid models							
5	Yes, infinitely deep	No	Yes, infinitely deep	No	No	Analytic	[37,62]
6	Yes, infinitely deep	No	Yes, infinitely deep	No	Yes	Analytic	[109,110]
						Experimental	[83,100]
						Semianalytic	[111]
7	No	No	Yes, finitely deep	Yes, finitely thick	No	Analytic	[14,16,112–117]
						Experimental	[14,118–124,147]
						Semianalytic	[13,15,17,26,125–128]
8	No	Yes, finitely thick	Yes, finitely deep	No	No	Analytic	[10]
						Experimental	[6,10–12,89,129–134]
						Semianalytic	[135–139]
9	No	Yes, finitely thick	Yes, finitely deep	No	Yes	Analytic	[32,51,140–142]
						Experimental	[143,144]
Three-fluid models							
10	Yes, infinitely deep	Yes, finitely thick	Yes, infinitely deep	No	Yes	Analytic	[7]
11	Yes, finitely deep	No	Yes, finitely deep	Yes, finitely thick	No	Numerical	[145,146]
Swell waves							
12							[5,6,8,53–56,148]

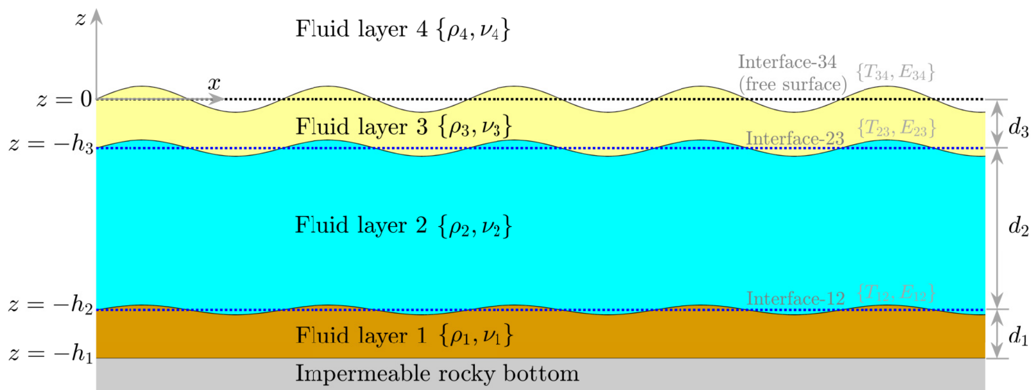

FIG. 1. Schematic of the multilayered fluid configuration representing the atmosphere-ocean system. The fourth fluid layer is infinitely deep. The fluid layers are numbered sequentially from bottom ($j = 1$) to top ($j = 4$). Here $h_1 = d_1 + d_2 + d_3$, $h_2 = d_2 + d_3$, and $h_3 = d_3$.

layer). This study aims to develop a generalized model for the spatial attenuation rates of gravity waves in such a system with stepwise stratification, by incorporating all the factors described in Sec. I A.

Here, we investigate freely propagating, monochromatic SGW with gently sloped crests and troughs, as depicted in Fig. 1. These waves exhibit swell-like characteristics: linearity, unidirectionality, nonbreaking behavior, and narrow-banded spectra. The fluid flow is laminar, incompressible, and two-dimensional. All fluids in this work are considered to be Newtonian, except for two specific cases (in these cases, we account for viscoelastic characteristics of the mud and oil layers by allowing their viscosities to be complex valued; see Sec. IV D). The fluid properties are uniform, and the interfaces are deemed to be elastic as a result of insoluble surfactant contamination. This work presents a comprehensive study on SGW attenuation, featuring the following key aspects:

(1) a semianalytic model, which combines mathematical analysis and numerical solutions obtained using MATLAB;
(2) the prediction of spatial attenuation rates, suitable for propagating waves;
(3) finite depths for three of the four layers, with values that cover a wide range of length scales (1 mm to 10 km);
(4) results for approximately three decades of wave frequency (0.005 Hz to 3 Hz), encompassing a wide range of corresponding timescales;
(5) elastic interfaces, which account for surfactant contamination;
(6) viscoelastic models for the mud and oil layers, reflecting their complex rheological behavior; and
(7) the effects of air dynamics on wave attenuation.

Our model has the following limitations:

(1) it is two-dimensional;
(2) it is not valid for nonlinear waves with large slopes;
(3) it does not consider soluble surfactants;
(4) it does not account for other complications at interfaces such as formation of emulsions;
(5) it does not account for spatiotemporal variations in fluid layer depths and thicknesses;
(6) it does not account for a nonuniform density field, such as that observed in the ocean, due to continuous stratification; and
(7) it does not account for mechanisms of energy dissipation other than those listed in Sec. I A.

While our model has limitations, its results are widely applicable to generic fluid systems beyond the air-oil-water-mud configuration. Notwithstanding these limitations, this study aims to contribute to the understanding of wave attenuation in multilayered fluid systems, demonstrate the potential of the proposed model for broad application, and lay the groundwork for future research. The remainder of this work is organized as follows. Section II presents the mathematical formulation, including the boundary value problem and derivation of the dispersion relation. Section III compares our model's predictions with previously published theoretical results and experimental data for select cases. Section IV presents attenuation rates for a wide range of frequencies and fluid layer depths, and examines the trends observed in the results. Section V provides an overview of the key findings and conclusions.

II. MATHEMATICAL FORMULATION

We consider linear, monochromatic, freely propagating, interfacial gravity waves in a system of immiscible fluids, as illustrated in Fig. 1. The system consists of four layers: mud ($j = 1$), water ($j = 2$), oil ($j = 3$), and air ($j = 4$). The (uniform) densities and kinematic viscosities of each layer are $\{\rho_j, \nu_j\}$, where $j = 1, 2, 3, 4$. Note that a system with generic fluids should satisfy the condition $\rho_4 \leqslant \rho_3 \leqslant \rho_2 \leqslant \rho_1$. The first three layers ($j = 1, 2, 3$)—mud, water, and oil—have uniform rest-state thicknesses (or depths) of d_1, d_2, and d_3, respectively, while the air layer is infinitely deep. The horizontal (x) and vertical (z) components of the velocity of fluid particles in the j^{th} layer are $\{u_j, w_j\}$, whereas p_j is the pressure field.

There are three interfaces that separate the four fluids. At each interface, the horizontal and vertical displacements of fluid particles (from their equilibrium positions) are $\{\xi_{ij}, \eta_{ij}\}$, where ij is the index pair that represents the interface between layers i and j. Each interface is assumed to be elastic (due to contamination by insoluble surfactants), and the rest-state interfacial tensions and elasticities are $\{T_{12}, E_{12}\}$, $\{T_{23}, E_{23}\}$, and $\{T_{34}, E_{34}\}$ respectively. Here we consider barotropic wave propagation, where interfacial displacements occur in phase with each other. To obtain the attenuation rates of wave amplitudes, we assume that they decay exponentially with distance along the horizontal direction of propagation. As outlined in Sec. I C, our analysis is applicable to the two-dimensional, laminar, incompressible flow of Newtonian fluids.

A. Linearized governing equations

The linearized governing equations for fluid flow are

$$\frac{\partial u_j}{\partial x} + \frac{\partial w_j}{\partial z} = 0, \tag{1}$$

$$\frac{\partial u_j}{\partial t} = -\frac{1}{\rho_j}\frac{\partial p_j}{\partial x} + \nu_j\left(\frac{\partial^2 u_j}{\partial x^2} + \frac{\partial^2 u_j}{\partial z^2}\right), \tag{2}$$

and

$$\frac{\partial w_j}{\partial t} = -\frac{1}{\rho_j}\frac{\partial p_j}{\partial z} + \nu_j\left(\frac{\partial^2 w_j}{\partial x^2} + \frac{\partial^2 w_j}{\partial z^2}\right), \tag{3}$$

where t represents time and subscript j represents the jth fluid layer.

B. Linearized boundary conditions

The linearized conditions at the five boundaries in the system are listed below.

(1) Impermeable bottom ($z = -h_1$): The no-slip condition at the bottom implies that

$$u_1 = 0, \tag{4}$$

$$w_1 = 0. \tag{5}$$

(2) Interface-12 ($z = -h_2$): For consistency with real flow conditions, it is required that the horizontal and vertical velocity profiles are continuous at the interface, and (respectively) equal to the time derivatives of corresponding particle displacements. Additionally, effects of interfacial

elasticity compensate for the difference in shear stresses on either side of the interface, while those of interfacial tension compensate for the difference in normal stresses. These conditions yield

$$u_1 = u_2 = \frac{\partial \xi_{12}}{\partial t}, \tag{6}$$

$$w_1 = w_2 = \frac{\partial \eta_{12}}{\partial t}, \tag{7}$$

$$\rho_1 \nu_1 \left[\frac{\partial u_1}{\partial z} + \frac{\partial w_1}{\partial x} \right] - \rho_2 \nu_2 \left[\frac{\partial u_2}{\partial z} + \frac{\partial w_2}{\partial x} \right] = E_{12} \frac{\partial^2 \xi_{12}}{\partial x^2}, \tag{8}$$

$$\left[p_2 - \rho_2 g \eta_{12} - 2\rho_2 \nu_2 \frac{\partial w_2}{\partial z} \right] - \left[p_1 - \rho_1 g \eta_{12} - 2\rho_1 \nu_1 \frac{\partial w_1}{\partial z} \right] = T_{12} \frac{\partial^2 \eta_{12}}{\partial x^2}, \tag{9}$$

where g is the acceleration due to gravity.

(3) Interface-23 ($z = -h_3$): Following the same line of reasoning applied to the first interface, we establish the following:

$$u_2 = u_3 = \frac{\partial \xi_{23}}{\partial t}, \tag{10}$$

$$w_2 = w_3 = \frac{\partial \eta_{23}}{\partial t}, \tag{11}$$

$$\rho_2 \nu_2 \left[\frac{\partial u_2}{\partial z} + \frac{\partial w_2}{\partial x} \right] - \rho_3 \nu_3 \left[\frac{\partial u_3}{\partial z} + \frac{\partial w_3}{\partial x} \right] = E_{23} \frac{\partial^2 \xi_{23}}{\partial x^2}, \tag{12}$$

$$\left[p_3 - \rho_3 g \eta_{23} - 2\rho_3 \nu_3 \frac{\partial w_3}{\partial z} \right] - \left[p_2 - \rho_2 g \eta_{23} - 2\rho_2 \nu_2 \frac{\partial w_2}{\partial z} \right] = T_{23} \frac{\partial^2 \eta_{23}}{\partial x^2}. \tag{13}$$

(4) Interface-34 (free surface; $z = 0$): Following the same line of reasoning applied to the first and second interfaces, we establish the following:

$$u_3 = u_4 = \frac{\partial \xi_{34}}{\partial t}, \tag{14}$$

$$w_3 = w_4 = \frac{\partial \eta_{34}}{\partial t}, \tag{15}$$

$$\rho_3 \nu_3 \left[\frac{\partial u_3}{\partial z} + \frac{\partial w_3}{\partial x} \right] - \rho_4 \nu_4 \left[\frac{\partial u_4}{\partial z} + \frac{\partial w_4}{\partial x} \right] = E_{34} \frac{\partial^2 \xi_{34}}{\partial x^2}, \tag{16}$$

$$\left[p_4 - \rho_4 g \eta_{34} - 2\rho_4 \nu_4 \frac{\partial w_4}{\partial z} \right] - \left[p_3 - \rho_3 g \eta_{34} - 2\rho_3 \nu_3 \frac{\partial w_3}{\partial z} \right] = T_{34} \frac{\partial^2 \eta_{34}}{\partial x^2}. \tag{17}$$

(5) At infinity ($z \to \infty$): Far from the free surface, velocity components vanish, which implies that

$$u_4 = 0, \tag{18}$$

$$w_4 = 0. \tag{19}$$

The boundary conditions presented above are in agreement with those employed in several works listed in Table I.

C. Velocity, pressure, and displacement fields

Following Dalrymple and Liu [13] and Rajan [7], we seek solutions of the form

$$\{u_j, w_j, p_j, \eta_{12}, \eta_{23}, \eta_{34}, \xi_{12}, \xi_{23}, \xi_{34}\} = \{\hat{u}_j(z), \hat{w}_j(z), \hat{p}_j(z), \hat{\eta}_{12}, \hat{\eta}_{23}, \hat{\eta}_{34}, \hat{\xi}_{12}, \hat{\xi}_{23}, \hat{\xi}_{34}\} \exp(\mathrm{i}\theta), \tag{20}$$

where $\theta = kx - \omega t$. Here, $\omega > 0$ is the frequency of oscillation, while $k = k_\mathrm{r} + \mathrm{i}k_\mathrm{i} \in \mathbb{C}$, where $k_\mathrm{r} \gtrless 0$ is the wave number (positive and negative values of k_r correspond to wave propagation in $+x$ and $-x$ directions) and k_i is the spatial rate of attenuation. Since the left-hand side of (20) consists of real-valued functions, only the real parts of corresponding right-hand side functions are relevant. For example, $u_j = \mathrm{Re}[\hat{u}_j(z)\exp(\mathrm{i}\theta)]$ and $\eta_{23} = \mathrm{Re}[\hat{\eta}_{23}\exp(\mathrm{i}\theta)]$. For conciseness, we will discard the "Re" notation henceforth, with the understanding that only the real part is considered in the relevant equations.

In this work, we consider only $k_\mathrm{r} > 0$; results for $k_\mathrm{r} < 0$ will be identical to the ones for $k_\mathrm{r} > 0$. It is important to note that wave attenuation requires $k_\mathrm{i} > 0$, indicating exponential decay with distance. Previous investigations on SGW attenuation have revealed that k_i is small compared to k_r (see [43,45]). Therefore, we look for solutions which satisfy the following conditions:

$$k_\mathrm{r} > 0, \quad k_\mathrm{i} > 0, \quad k_\mathrm{i} \ll k_\mathrm{r}. \tag{21}$$

The third condition in (21) aligns with our objective of identifying the least-damped wave mode, as supported by the findings in [7,12,32,38,44,45,49,51,110,138,149,150], which suggest that, for gravity waves, the spatial attenuation rate could be one to three orders of magnitude smaller than the wave number. Other modes, such as those associated with Marangoni waves for which $k_\mathrm{i} \sim k_\mathrm{r}$ are considered elsewhere (see [50,149]).

Substituting expressions for u_j and w_j from (20) in (1), we obtain

$$\hat{u}_j(z) = \frac{\mathrm{i}}{k}\left\{\frac{\mathrm{d}\hat{w}_j(z)}{\mathrm{d}z}\right\}. \tag{22}$$

Using (20) and (22) in the x-momentum equation, (2), we obtain

$$\hat{p}_j(z) = \frac{\rho_j \nu_j}{k^2}\left[\frac{\mathrm{d}^3\hat{w}_j(z)}{\mathrm{d}z^3} - m_j^2\frac{\mathrm{d}\hat{w}_j(z)}{\mathrm{d}z}\right], \tag{23}$$

where

$$m_j = \pm\sqrt{k^2 - \mathrm{i}\frac{\omega}{\nu_j}}. \tag{24}$$

Using (20), (22), and (23) in the z-momentum equation, (3), yields the ordinary differential equation

$$\frac{\mathrm{d}^4\hat{w}_j(z)}{\mathrm{d}z^4} - \left(m_j^2 + k^2\right)\frac{\mathrm{d}^2\hat{w}_j(z)}{\mathrm{d}z^2} + k^2 m_j^2\,\hat{w}_j(z) = 0, \tag{25}$$

which can be solved to obtain

$$\hat{w}_1(z) = \mathrm{C}_1\sinh[k(z+h_1)] + \mathrm{C}_2\cosh[k(z+h_1)] + \mathrm{C}_3\exp[m_1(z+h_1)] + \mathrm{C}_4\exp[-m_1(z+h_1)], \tag{26}$$

$$\hat{w}_2(z) = \mathrm{C}_5\sinh[k(z+h_2)] + \mathrm{C}_6\cosh[k(z+h_2)] + \mathrm{C}_7\exp[m_2(z+h_2)] + \mathrm{C}_8\exp[-m_2(z+h_2)], \tag{27}$$

$$\hat{w}_3(z) = \mathrm{C}_9\sinh[k(z+h_3)] + \mathrm{C}_{10}\cosh[k(z+h_3)] + \mathrm{C}_{11}\exp[m_3(z+h_3)] + \mathrm{C}_{12}\exp[-m_3(z+h_3)], \tag{28}$$

$$\hat{w}_4(z) = \mathrm{C}_{13}\exp[-kz] + \mathrm{C}_{14}\exp[-m_4 z]. \tag{29}$$

To obtain (29), we found the general solution of (25) for $j = 4$, assumed that $k_\mathrm{r} > 0$ and $m_{4\mathrm{r}} := \mathrm{Re}(m_4) > 0$ without loss of generality, and invoked the condition (19). One may note that there are two possible values of m_4 which can be obtained from (24). Of these two, the one with negative real part [Re(m_4) < 0] will invalidate (19). Therefore, we will pick the one with $m_{4r} := \mathrm{Re}(m_4) > 0$. Using (22) and (26)–(29), we obtain

$$\hat{u}_1(z) = \frac{\mathrm{i}}{k}\{\mathrm{C}_1\, k\, \cosh[k(z+h_1)] + \mathrm{C}_2\, k\, \sinh[k(z+h_1)] + \mathrm{C}_3\, m_1 \exp[m_1(z+h_1)] - \mathrm{C}_4\, m_1 \exp[-m_1(z+h_1)]\}, \tag{30}$$

$$\hat{u}_2(z) = \frac{\mathrm{i}}{k}\{\mathrm{C}_5\, k\, \cosh[k(z+h_2)] + \mathrm{C}_6\, k\, \sinh[k(z+h_2)] + \mathrm{C}_7\, m_2 \exp[m_2(z+h_2)] - \mathrm{C}_8\, m_2 \exp[-m_2(z+h_2)]\}, \tag{31}$$

$$\hat{u}_3(z) = \frac{\mathrm{i}}{k}\{\mathrm{C}_9\, k\, \cosh[k(z+h_3)] + \mathrm{C}_{10}\, k\, \sinh[k(z+h_3)] + \mathrm{C}_{11}\, m_3 \exp[m_3(z+h_3)] - \mathrm{C}_{12}\, m_3 \exp[-m_3(z+h_3)]\}, \tag{32}$$

$$\hat{u}_4(z) = -\frac{\mathrm{i}}{k}\{\mathrm{C}_{13}\, k \exp[-kz] + \mathrm{C}_{14}\, m_4 \exp[-m_4 z]\}. \tag{33}$$

Using (23) and (26)–(29), we obtain

$$\hat{p}_1(z) = \frac{\rho_1\nu_1}{k^2}\left(k^2 - m_1^2\right)\{\mathrm{C}_1\, k\, \cosh[k(z+h_1)] + \mathrm{C}_2\, k\, \sinh[k(z+h_1)]\}, \tag{34}$$

$$\hat{p}_2(z) = \frac{\rho_2\nu_2}{k^2}\left(k^2 - m_2^2\right)\{\mathrm{C}_5\, k\, \cosh[k(z+h_2)] + \mathrm{C}_6\, k\, \sinh[k(z+h_2)]\}, \tag{35}$$

$$\hat{p}_3(z) = \frac{\rho_3\nu_3}{k^2}\left(k^2 - m_3^2\right)\{\mathrm{C}_9\, k\, \cosh[k(z+h_3)] + \mathrm{C}_{10}\, k\, \sinh[k(z+h_3)]\}, \tag{36}$$

$$\hat{p}_4(z) = \frac{\rho_4\nu_4}{k}\left(m_4^2 - k^2\right)\mathrm{C}_{13} \exp(-kz). \tag{37}$$

Substituting (26)–(28) in (7), (11), and (15) and integrating, we obtain

$$\hat{\eta}_{12} = \frac{\mathrm{i}}{\omega}[\mathrm{C}_1\, \sinh(kd_1) + \mathrm{C}_2\, \cosh(kd_1) + \mathrm{C}_3 \exp(m_1 d_1) + \mathrm{C}_4 \exp(-m_1 d_1)], \tag{38}$$

$$\hat{\eta}_{23} = \frac{\mathrm{i}}{\omega}[\mathrm{C}_5\, \sinh(kd_2) + \mathrm{C}_6\, \cosh(kd_2) + \mathrm{C}_7 \exp(m_2 d_2) + \mathrm{C}_8 \exp(-m_2 d_2)], \tag{39}$$

$$\hat{\eta}_{34} = \frac{\mathrm{i}}{\omega}[\mathrm{C}_9\, \sinh(kd_3) + \mathrm{C}_{10}\, \cosh(kd_3) + \mathrm{C}_{11} \exp(m_3 d_3) + \mathrm{C}_{12} \exp(-m_3 d_3)]. \tag{40}$$

Substituting (30)–(32) in (6), (10), and (14) and integrating, we obtain

$$\hat{\xi}_{12} = \frac{-1}{\omega k}[\mathrm{C}_1\, k\, \cosh(kd_1) + \mathrm{C}_2\, k\, \sinh(kd_1) + \mathrm{C}_3\, m_1 \exp(m_1 d_1) - \mathrm{C}_4\, m_1 \exp(-m_1 d_1)], \tag{41}$$

$$\hat{\xi}_{23} = \frac{-1}{\omega k}[\mathrm{C}_5\, k\, \cosh(kd_2) + \mathrm{C}_6\, k\, \sinh(kd_2) + \mathrm{C}_7\, m_2 \exp(m_2 d_2) - \mathrm{C}_8\, m_2 \exp(-m_2 d_2)], \tag{42}$$

$$\hat{\xi}_{34} = \frac{-1}{\omega k}[\mathrm{C}_9\, k\, \cosh(kd_3) + \mathrm{C}_{10}\, k\, \sinh(kd_3) + \mathrm{C}_{11}\, m_3 \exp(m_3 d_3) - \mathrm{C}_{12}\, m_3 \exp(-m_3 d_3)]. \tag{43}$$

D. The dispersion relation and solution procedure

The velocity, pressure, and displacement fields can be determined by substituting (26)–(43) in (20). The resulting expressions can then be substituted in the linearized boundary conditions (4)–(17) to obtain a system of fourteen linear equations involving the variables $\{\mathrm{C}_\ell\}_{\ell=1}^{14}$. This equation system can be expressed in matrix form as $[\mathcal{A}]_{14\times 14}[\mathcal{C}]_{14\times 1} = 0$, where $\mathcal{C}$ is a 14×1 column-matrix comprising the elements $\{\mathrm{C}_\ell\}_{\ell=1}^{14}$. The 14×14 elements of the coefficient matrix, $\mathcal{A}$, are presented in the Appendix.

This problem involves four main categories of parameters: the set of all fluid properties, $S_{\mathrm{fp}} = \{\rho_1, \rho_2, \rho_3, \rho_4, \nu_1, \nu_2, \nu_3, \nu_4\}$; the set of all interface properties, $S_{\mathrm{ip}} = \{T_{12}, T_{23}, T_{34}, E_{12}, E_{23}, E_{34}\}$; the set of all geometric dimensions, $S_{\mathrm{gd}} = \{d_1, d_2, d_3\}$; and wave-related variables, $\{\omega, k\}$. Among these nineteen, only k is complex-valued (if any fluid is viscoelastic rather than Newtonian, its viscosity would also be complex-valued). Nontrivial solutions of the equation system $[\mathcal{A}]_{14\times 14}[\mathcal{C}]_{14\times 1} = 0$ are obtained when $|\mathcal{A}| = 0$, which yields the dispersion relation, $\omega = \omega(k; S)$, where $S = S_{\mathrm{fp}} \cup S_{\mathrm{ip}} \cup S_{\mathrm{gd}}$. For given values of ω and the parameters in S, one may obtain multiple values of $k = k_{\mathrm{r}} + \mathrm{i}k_{\mathrm{i}}$ (solutions) which satisfy $|\mathcal{A}| = 0$. Of these solutions, the ones that are physically realistic are those that satisfy the conditions in (21).

The multiple physically realistic solutions (of $|\mathcal{A}| = 0$) correspond to various modes of wave propagation. Traditionally, analyses of gravity wave attenuation have focused on the mode with (absolute value of) wave number, $|k|$, closest to the inviscid wave number, $k_0 > 0$ (k_0 is the wave number that satisfies the inviscid dispersion relation for gravity waves in a fluid system devoid of surfactants), allowing one to use the ansatz $k = k_0(1 + \varepsilon)$, where $\varepsilon \in \mathbb{C}$ and $|\varepsilon| \ll 1$ (see [7,110,129,137,138,149] for similar propositions). The inviscid dispersion relation takes different forms depending on the system under consideration. For instance, it is

$$\omega^2 = gk_0 \tanh(k_0 h) \tag{44}$$

for SGWs in a system comprising a single fluid layer of depth h, and

$$\omega^2 = gk_0(\rho_\ell - \rho_u)\left[\frac{\tanh(k_0 h_\ell)\tanh(k_0 h_u)}{\rho_u \tanh(k_0 h_\ell) + \rho_\ell \tanh(k_0 h_u)}\right] \tag{45}$$

for interfacial gravity waves in a two-fluid system comprising an upper layer of density ρ_u and depth h_u, and a lower layer of density ρ_ℓ and depth h_ℓ. Note that (45) reduces to (44) when the upper fluid is neglected ($\rho_u = 0$) and h_ℓ is replaced with h in the two-fluid system. For a given value of ω, the corresponding value of k_0 varies depending on the chosen dispersion relation; for example, a fixed value of ω can result in different k_0 values depending on whether one uses (44) or (45).

In a fluid system with n interfaces, wave propagation occurs in n modes: 1 barotropic and $n - 1$ baroclinic. Here we are interested in the barotropic mode of wave propagation, which is the fastest of all modes (see [7,151,152]). Therefore, of the multiple physically realistic solutions, we pursue the one with the lowest value of k_{r} to maximize the phase velocity, $c_{\mathrm{p}} \sim \omega/k_{\mathrm{r}}$ (for a fixed value of ω). The inviscid dispersion relation for SGW in a single-fluid system, (44), can be derived as a limiting case of that for a multilayered fluid system. This reduction is accomplished by setting the densities of all but one fluid layer in the multilayered system to zero. However, this simplification holds only if wave propagation in the multilayered system occurs in the barotropic mode (see [7] for a similar result). When a multilayered fluid system is reduced to a single-fluid system, the baroclinic mode vanishes, but the barotropic mode persists, and the corresponding dispersion relation simplifies to $\omega^2 = gk_0 \tanh(k_0 h)$, implying that k_0 is the inviscid wave number associated with the barotropic mode of propagation in multilayered fluid systems.

For a given frequency, ω, and a unique set of parameter values in S, we aim to determine a single value for $k = k_{\mathrm{r}} + \mathrm{i}k_{\mathrm{i}}$ that meets the following criteria: (a) it satisfies $|\mathcal{A}| = 0$, (b) it is physically realistic and complies with all conditions specified in (21), and (c) it has the lowest value of k_{r} (which corresponds to the barotropic mode). Since it is difficult to obtain analytic solutions, we employ the inbuilt solver `vpasolve` in MATLAB, which requires the specification of an initial guess value to obtain an exact numerical solution, $k = k_{\mathrm{r}} + \mathrm{i}k_{\mathrm{i}}$. Here we aim to obtain the solution having the lowest value of k_{r}, so it is logical to specify the inviscid wave number corresponding to the barotropic mode of propagation in the multilayered fluid system as the initial guess value when obtaining the numerical solution using `vpasolve`. However, obtaining an analytic expression for k_0 in the multilayered system is challenging, due to the multitude of parameters involved. Therefore, we calculate k_0 from the single-fluid dispersion relation (which corresponds to the barotropic mode), (44), by letting $h = d_1 + d_2 + d_3$; and provide this k_0 as the initial guess value—for all cases in this work. When provided with this initial guess value, we expect `vpasolve` to yield the exact solution

$k = k_{\rm rl} + {\rm i}k_{\rm i}$, where $k_{\rm rl}$ represents the lowest value of $k_{\rm r}$. To verify this expectation, we compute other numerical solutions (and confirm that their real parts are all greater than $k_{\rm rl}$) following the steps listed below.

(1) Specify the wave frequency, ω (>0).

(2) Specify the numerical values of all parameters in the set S.

(3) Obtain a solution (numerical value of $k = k_{\rm r} + {\rm i}k_{\rm i}$ that satisfies $|\mathcal{A}| = 0$) using the inbuilt solver `vpasolve` in MATLAB, by providing any initial guess value other than the k_0 obtained from (44). Reject this solution even if any one of the three conditions in (21) is not satisfied. If the solution is rejected, repeat the process until a solution that satisfies all the three conditions in (21) is obtained.

(4) Repeat step 3 several times (we chose to repeat it at least five times) to obtain multiple solutions.

(5) Check if each of these solutions (computed in steps 3 and 4) has a value of $k_{\rm r}$ which is greater than $k_{\rm rl}$.

For every case considered in this work, we followed the steps above to ensure that the solution of interest is the one which has the lowest value of $k_{\rm r}$. As expected, the inbuilt solver `vpasolve` consistently yielded the solution ($k = k_{\rm rl} + {\rm i}k_{\rm i}$) with the lowest value of $k_{\rm r}$ when provided with the initial guess value of k_0 obtained from (44) by letting $h = d_1 + d_2 + d_3$. We report that none of the several initial guess values provided in `vpasolve` yielded a solution $k = k_{\rm r} + {\rm i}k_{\rm i}$ with $k_{\rm r} < k_{\rm rl}$ (for each case, we also obtained a solution using `vpasolve` with an initial guess value of ω^2/g, and found that this exercise yielded the solution, $k = k_{\rm rl} + {\rm i}k_{\rm i}$, which is same as the one obtained using `vpasolve` with the initial guess value of k_0 from (44) by letting $h = d_1 + d_2 + d_3$.) The results obtained in some cases have also been validated against previously published theoretical and experimental data (see Sec. III for details).

III. VALIDATION

Before proceeding to obtain solutions for various systems of interest, we validate the current model by producing results for a few cases and comparing them with previously published results from Gade [14,153], Dalrymple and Liu [13], Rajan [7], Jiang [154], and Jain and Mehta [20]. These studies examined wave attenuation in two-layered and three-layered fluid systems. For comparison, we adapt our model to produce results for wave attenuation by modifying the values of densities, viscosities, and depths in the four-layered fluid system (see Fig. 1), so that it effectively reduces to either a two-layered or three-layered fluid system. Table II lists the cases considered for validation, and the numerical values of various parameters used to obtain results presented in Figs. 2–5. In cases where two adjacent fluid layers have the same densities and same viscosities, the interface between them ceases to exist. Such identical, adjacent fluid layers can be replaced with a single homogeneous fluid layer whose depth equals the sum of depths of the individual layers. For instance, in the first case of Table II (corresponding to Fig. 2), the second and third fluid layers are identical ($\rho_2 = \rho_3$ and $\nu_2 = \nu_3$), and can thus be replaced with a single, homogeneous fluid layer of density ρ_2, viscosity ν_2, and depth $d_2 + d_3$. This exercise is done to reduce the current four-layered fluid system (see Fig. 1) to a two-layered fluid system (note that $\rho_4 = 0$ for this case). In cases where $\rho_4 = 0$, the fourth fluid layer in Fig. 1 is neglected (or replaced with a vacuum). For the cases in Table II, tensions and elasticites of all interfaces are zero.

Figure 2 presents the results for a system comprising kerosene and water-sugar solution. The two panels in Fig. 2 present the wave number and attenuation rate as functions of the depth of the water-sugar-solution layer. [Figure 2 of Dalrymple and Liu [13] has ordinate values that are one order of magnitude higher than those in our Fig. 2(b). However, Gade's Ph.D. thesis [153] confirms that our values in Fig. 2(b) are correct, indicating a typographical error in Fig. 2 of Dalrymple and Liu [13].] Gade's experimental data (circles in Fig. 2) were obtained from a 6 ft × 6 in × 1 ft wavetank, comprising kerosene overlying a water-sugar solution base. As reported in Gade's thesis [153], the discrepancies between their experimental and analytic results (black circles and the green dotted curves in Fig. 2) are likely due to wave reflection from the tank's ends, frictional resistance

TABLE II. Numerical values of parameters used to obtain results in Figs. 2–5.

Fig. no.	ω (rad/s)	ρ_1 (kg/m^3)	ν_1 (m^2/s)	ρ_2 (kg/m^3)	ν_2 (m^2/s)	ρ_3 (kg/m^3)	ν_3 (m^2/s)	ρ_4 (kg/m^3)	ν_4 (m^2/s)	d_1 (m)	d_2 (m)	d_3 (m)	Values obtained from
2	4.488	1504	2.6×10^{-3}	859.3	2.42×10^{-6}	859.3	2.42×10^{-6}	0	0	0–0.255	0.0381	0	[13,14]
		(water-sugar solution)		(kerosene)		(kerosene)		(vacuum)					
3	1.2566	1800	1×10^{-1}	1028	2.6×10^{-6}	1028	2.6×10^{-6}	0	0	0.1–5.6	4	0	[13]
		(thick fluidized mud)		(sea water)		(sea water)		(vacuum)					
4	0.402–20.9	1000	1×10^{-6}	1000	1×10^{-6}	900	1×10^{-4}	1.2	15×10^{-6}	10^2–10^4	0	10^{-6}–10^{-3}	[7]
		(water)		(water)		(oil)		(air)					
5	3–12.56	1200	Variable	1000	1×10^{-6}	1000	1×10^{-6}	0	0	0.12, 0.18	0.14–0.16	0	[20]
		(Newtonian/viscoelastic mud)		(water)		(water)		(vacuum)					

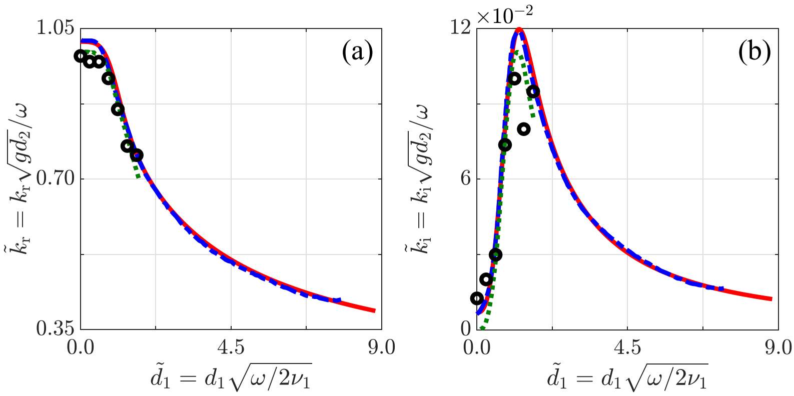

FIG. 2. The (a) dimensionless wave number, $\tilde{k}_{\mathrm{r}}$, and (b) dimensionless attenuation rate, $\tilde{k}_{\mathrm{i}}$, as functions of the dimensionless depth, $\tilde{d}_1$, of the first fluid layer in a system composed of kerosene and water-sugar solution. Black circles and green dotted curves represent the experimental and analytic results of Gade [14], and were obtained by digitizing their Figs. 3 and 4. The blue dash-dotted curves represent the analytic results of Dalrymple and Liu [13] and were obtained by digitizing their Figs. 2 and 3. The red solid curves represent results of the current model. Numerical values of parameters used to obtain results are available in Table II.

along the sidewalls, and deviations of the observed wave profile from the assumed sinusoidal shape.

Figure 3 presents a comparison of our analytic results with those from Dalrymple and Liu [13] for a fluid system comprising sea water and thick fluidized mud. As illustrated in both Figs. 2 and 3, our results show good agreement with the experimental and analytic results from previous studies. In both figures, one may note that $k_{\mathrm{i}} \ll k_{\mathrm{r}}$, reaffirming the third condition in (21) and providing a theoretical basis for our focus on the least-damped wave mode. The results also demonstrate an inverse relationship between wave number and lower-layer depth, as anticipated. Furthermore, the attenuation rate, k_{i}, exhibits a nonmonotonic dependence on d_1, which will be examined in greater detail in subsequent sections.

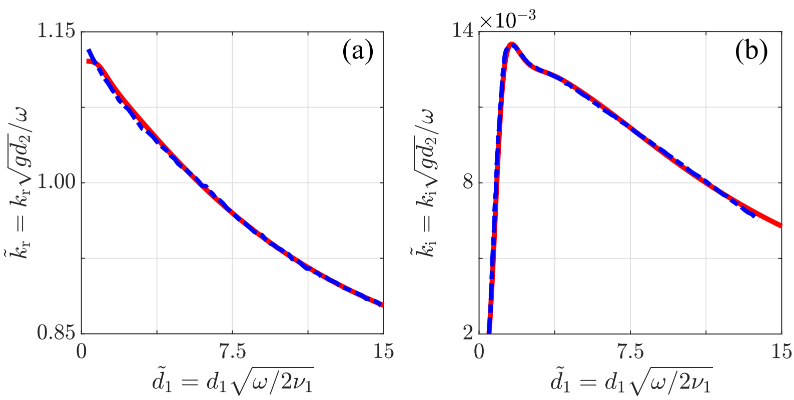

FIG. 3. The (a) dimensionless wave number, $\tilde{k}_{\mathrm{r}}$ and (b) dimensionless attenuation rate, $\tilde{k}_{\mathrm{i}}$, as functions of the dimensionless depth, $\tilde{d}_1$, of the first fluid layer in a system composed of sea water and thick fluidized mud. The blue dashed-dotted curves represent results from Dalrymple and Liu [13], obtained by digitizing their Figs. 6 and 7. The red solid curves represent results of the current model. Numerical values of parameters used to obtain results are available in Table II.

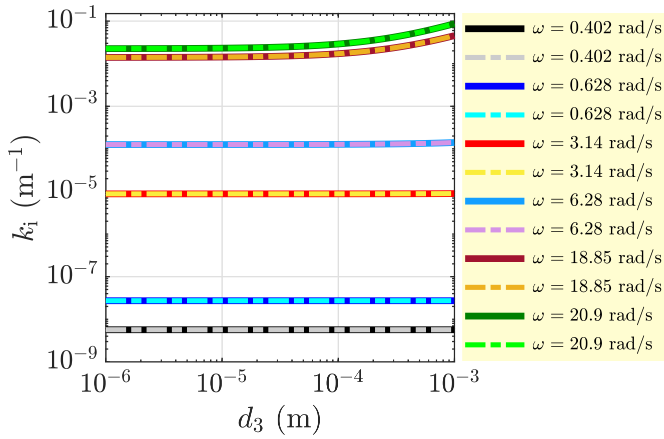

FIG. 4. Spatial attenuation rates of waves in an air-oil-water system. Dashed-dotted curves represent results obtained using the current model, whereas solid curves represent results obtained using the three-fluid model of Rajan [7]. Numerical values of parameters used to obtain results are available in Table II. For consistency with the three-fluid model of [7], which considers a semi-infinitely deep water layer, here we let (i) $d_1 = 10$ km, (ii) $d_1 = 1$ km, and (iii) $d_1 = 0.1$ km to produce results for waves of frequencies (i) 0.402 rad/s, 0.628 rad/s; (ii) 3.14 rad/s, 6.28 rad/s; and (iii) 18.85 rad/s, 20.9 rad/s respectively; ensuring that $k_r d_1 \gg 1$, which represents the deep-fluid limit. Here d_3 is the thickness of oil layer.

Figure 4 presents the results for a system composed of a semi-infinitely deep air layer, a finitely deep oil layer of thickness d_3, and a semi-infinitely deep water layer. These results show that the oil layer's thickness does not have any considerable impact on wave attenuation when frequencies are low. For high-frequency gravity waves (see the top two solid or dashed-dotted curves in Fig. 4), the attenuation rate increases by about one order of magnitude when the oil-layer's thickness increases from 1 μm to 1 mm. In a system with an oil layer of specified thickness, the attenuation rate is larger for a wave of larger frequency (for the ranges of values of all parameters considered here), implying that shorter waves experience more damping than longer ones. However, this result may not be true if one considers a wider frequency range, wherein the attenuation rate could likely be a nonmonotonic function of wave frequency (or wave number).

From Fig. 4, it is evident that the results obtained using the current model are in excellent agreement with those obtained using the three-fluid model of Rajan [7]. (To obtain spatial attenuation rates using the three-fluid model of [7], we assumed ω to be real-valued and k to be complex-valued.) A significant difference between the three-fluid model in [7] and the current model is that the former is limited by the condition $k_r d_3 \ll 1$, which was required to provide an explicit mathematical expression for the attenuation rate. This condition is not required here because we compute the attenuation rates numerically after obtaining mathematical expressions (see the Appendix) initially (rather than obtaining complete mathematical expressions for the attenuation rate without the aid of numerics, such as was done in [7]), so it is possible to investigate the dynamics of oil layers with large thicknesses using this current model. In fact, this was one of the reasons why we pursued to generalize the three-fluid model of [7]. The condition $k_r d_3 \ll 1$ indicates that the oil layer is extremely thin, so the physical implication here is that the fluid particles (in the oil layer) are restricted in terms of their ability to complete full orbits. Another significant difference between the three-fluid model of [7] and the current model is that the former assumed semi-infinite depths for two of the three fluid layers. The current model accounts for the finite depths of three of the four fluid layers, so it is a generalization of the three-fluid model; here, the water layer has a finite depth and overlies a mud layer of finite depth.

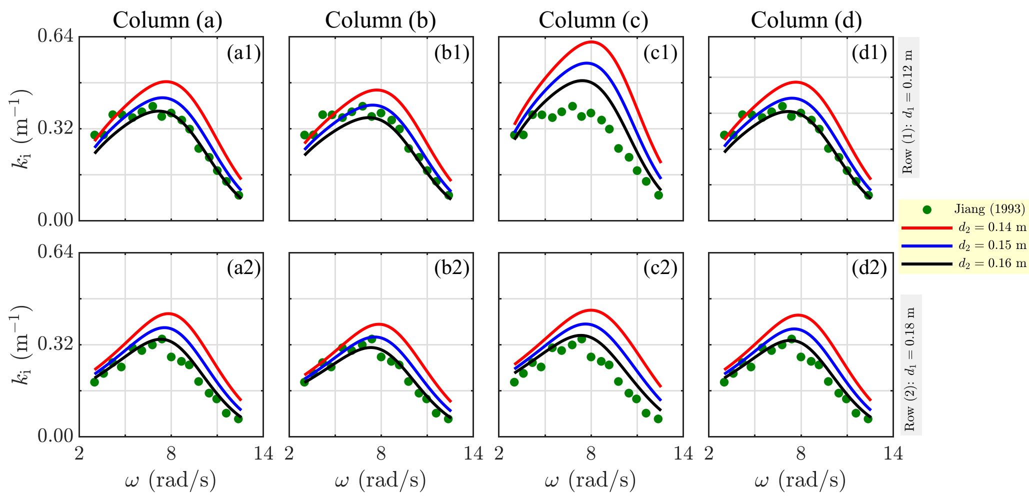

FIG. 5. The spatial attenuation rate, $k_{\rm i}$, as a function of the frequency, ω, of waves in a water-mud system. Rows 1 and 2 correspond to two different depths of the mud layer. The three curves in each panel represent results obtained using the present model and correspond to three different depths of the water layer. The green circles in each panel represent the experimental measurements of Jiang [154], obtained by digitizing figure 5 of [20]. Columns (a)–(d) present results obtained using (i) a Newtonian model for mud with $\nu_1 = 1.67 \times 10^{-2}$ m^2/s; (ii) a Newtonian model for mud with $\nu_1 = 1.5 \times 10^{-2}$ m^2/s; (iii) Maxwell's viscoelastic model for mud, $\nu_1 := \nu_{1\rm M}(1 + {\rm i}\omega\lambda)/(1 + \omega^2\lambda^2)$, with $\nu_{1\rm M} = 0.01667$ m^2/s, $\lambda = 0.0667$ s; and (iv) Jeffrey's viscoelastic model for mud, $\nu_1 := \nu_{1\rm J}(1 + {\rm i}\omega\lambda_2)/(1 + {\rm i}\omega\lambda_1)$, with $\nu_{1\rm J} = 0.0175$ m^2/s, $\lambda_1 = 1.07$ s, $\lambda_2 = 1$ s. Other numerical values used to obtain these results are available in Table II.

Figure 5 presents the results for a water-mud system, whose properties are available in the last row of Table II. Spatial attenuation rates are presented as functions of the frequency for various values of the mud-layer viscosity, ν_1, and two different values of its thickness, d_1 (see rows 1 and 2). The red, blue, and black solid curves in each panel represent results for different depths of the water layer. Panels in columns (a) and (b) present results for wave attenuation obtained by considering the mud layer to be Newtonian, whereas those in columns (c) and (d) present results for wave attenuation obtained by considering the mud layer to be viscoelastic. To obtain results for wave attenuation in a system with a viscoelastic fluid layer, we used governing equations valid for a Newtonian fluid, but simply allowed the fluid viscosity to be complex-valued. The complex-valued viscosities we used here are

$$\nu_j := \nu_{j\rm M}\left(\frac{1 + {\rm i}\omega\lambda}{1 + \omega^2\lambda^2}\right) \quad \text{and} \quad \nu_j := \nu_{j\rm J}\left(\frac{1 + {\rm i}\omega\lambda_2}{1 + {\rm i}\omega\lambda_1}\right), \tag{46}$$

which correspond to the Maxwell (subscript M) and Jeffrey (subcript J) models for viscoelatic fluids, where λ and $\{\lambda_1, \lambda_2\}$ are time constants of the fluid material, j. To obtain results for wave attenuation in a system with viscoelastic mud layer [results presented in columns (c) and (d) of Fig. 5], we let $j = 1$ in (46).

Results in Fig. 5 show that the wave attenuation is a nonmonotonic function of the frequency (within the ranges of values of parameters considered here), which is consistent with the results in [32]. To comprehend this nonmonotonic behavior, we classified the results into three regimes by comparing the various length scales relevant to the problem. The results of this exercise are presented in Table III, from which we observe that (for a system with fixed values of fluid properties and layer depths, see for instance the black curve in either panel (a1) or panel (a2) of Fig. 5) the maximum attenuation rate occurs when $k_{\rm r}^{-1} \sim d_1 > \delta_1$. The condition $k_{\rm r} d_1 \sim 1$ indicates that the

TABLE III. Numerical values of various length scales corresponding to the black curves in panels (a1) and (a2) of Fig. 5: boundary layer thickness, $\delta_j := \sqrt{2\nu_j/\omega}$, and the wavelength, k_r^{-1}. Here $\tilde{d}_1 = d_1/\delta_1$.

	Results for the lowest value of ω (=3 rad/s)	Results for the value of ω that maximizes k_i	Results for the largest value of ω (=12.56 rad/s)
Results for the black curve in panel (a1) of Fig. 5 for which $d_1 = 0.12$ m and $d_2 = 0.16$ m	$\omega = 3$ rad/s $k_r = 2.18$ m^{-1} $k_r^{-1} = 0.459$ m $\delta_1 = 0.106$ m $\delta_2 = 8.16 \times 10^{-4}$ m $k_r d_1 = 0.262$ $\tilde{d}_1 = 1.13$	$\omega \sim 7.206$ rad/s $k_r = 6.06$ m^{-1} $k_r^{-1} = 0.165$ m $\delta_1 = 0.0681$ m $\delta_2 = 5.27 \times 10^{-4}$ m $k_r d_1 = 0.727$ $\tilde{d}_1 = 1.76$	$\omega = 12.56$ rad/s $k_r = 16.1$ m^{-1} $k_r^{-1} = 0.0621$ m $\delta_1 = 0.0516$ m $\delta_2 = 3.99 \times 10^{-4}$ m $k_r d_1 = 1.93$ $\tilde{d}_1 = 2.32$
Results for the black curve in panel (a2) of Fig. 5 for which $d_1 = 0.18$ m and $d_2 = 0.16$ m	$\omega = 3$ rad/s $k_r = 1.90$ m^{-1} $k_r^{-1} = 0.526$ m $\delta_1 = 0.106$ m $\delta_2 = 8.16 \times 10^{-4}$ m $k_r d_1 = 0.342$ $\tilde{d}_1 = 1.70$	$\omega \sim 7.302$ rad/s $k_r = 5.85$ m^{-1} $k_r^{-1} = 0.171$ m $\delta_1 = 0.0676$ m $\delta_2 = 5.23 \times 10^{-4}$ m $k_r d_1 = 1.05$ $\tilde{d}_1 = 2.66$	$\omega = 12.56$ rad/s $k_r = 16.1$ m^{-1} $k_r^{-1} = 0.0621$ m $\delta_1 = 0.0516$ m $\delta_2 = 3.99 \times 10^{-4}$ m $k_r d_1 = 2.90$ $\tilde{d}_1 = 3.49$
Classification	Regime I: $k_r d_1 < 1$ $1.1 < d_1/\delta_1 < 1.7$ $k_r^{-1} > d_1 > \delta_1$	Regime II: $k_r d_1 \sim 1$ $1.7 < d_1/\delta_1 < 2.7$ $k_r^{-1} \sim d_1 > \delta_1$	Regime III: $k_r d_1 > 1$ $2.3 < d_1/\delta_1 < 3.5$ $d_1 > k_r^{-1} \sim \delta_1$

mud layer is of optimum depth which is neither too shallow nor too deep. The velocity gradients and the resulting shear within a fluid layer are likely to be stronger when $k_r d_1 \sim 1$ than they are when $k_r d_1 \gtrless 1$, which seems to explain why the attenuation rate reaches a maximum [in the black curves in panels (a1) and (a2) of Fig. 5 and Table III] when $k_r d_1 \sim 1$. For the results presented in Table III, we focused on the black curves in panels (a1) and (a2) of Fig. 5, but these arguments apply individually to each of the three curves in all panels of Fig. 5. See Sec. IV F for more discussion on the maximization of attenuation rates.

For specified values of the frequency (ω) and mud-layer thickness (d_1) in Fig. 5, the attenuation rate increases as the water-layer depth decreases (within the ranges of values considered here), consistent with the results of Jain and Mehta [20]. Wave attenuation rates obtained using viscoelastic fluid models for mud deviate only slightly from those obtained using a Newtonian fluid model for mud (compare results in columns (c) and (d) with those in columns (a) and (b) of Fig. 5), indicating that mud is likely Newtonian under these conditions and within the ranges of values of parameters considered here. Finally, we highlight the agreement between the results obtained using the current model and the experimental data of Jiang [154] (compare the solid curves and the dots in Fig. 5), which reaffirmed our confidence in the current model.

IV. PARAMETRIC STUDIES

There are several variables involved in this problem, which are included in the set S (see Sec. II D). This provides a solid basis for conducting extensive parametric studies, the results of which will help us gain insights into the various factors that affect wave attenuation. A summary of the parametric studies considered in this work is presented in Table IV. We present the results in multiple subsections below.

TABLE IV. Summary of parametric studies considered in this work. CV = complex-valued.

Fig. no.	ω (rad/s)	ρ_1 (kg/m^3)	ρ_2 (kg/m^3)	ρ_3 (kg/m^3)	ρ_4 (kg/m^3)	ν_1 (m^2/s)	ν_2 (m^2/s)	ν_3 (m^2/s)	ν_4 (m^2/s)	d_1 (m)	d_2 (m)	d_3 (m)	T_{12} (mN/m)	T_{23} (mN/m)	T_{34} (mN/m)	E_{12} (mN/m)	E_{23} (mN/m)	E_{34} (mN/m)
6	6.283	1200	1030	850	0	0.015	10^{-6}	10^{-4}	0	0.15	0.45-0.85	$0-0.76$	0	0	0	0	0	0
7	6.283	1200	1030	850	0	0.015	10^{-6}	10^{-4}	0	$0.025-0.75$	0.7275	$0-0.76$	0	0	0	0	0	0
8	6.283	1200	1030	850	0	0.015	10^{-6}	$10^{-4}-10^{-3}$	0	0.15	0.45	$0-2$	0	0	0	0	0	0
9	$0.2-12.56$	1200	1030	850	0	0.015	10^{-6}	10^{-4}	0	2	4	$0-2$	0	0	0	0	0	0
10	$0.3-1.8$	1200	1030	850	0	0.015	10^{-6}	10^{-4}	0	2	$4-5000$	$0-2$	0	0	0	0	0	0
11, 12	$0.037-3.7$	1200	1030	900	0	0.015	10^{-6}	10^{-4}	0	$0-1$	1	0.1	0	0	0	0	0	0
13	$3.14-18.85$	1200	1030	900	0	0.015	10^{-6}	10^{-4}	0	0.3	1.5	$10^{-4}-10^{-2}$	0, 50	0, 50	0, 20	0, 40	0, 40	0, 10
14	$3.14-18.85$	1200	1030	900	0	0.015	10^{-6}	10^{-4}	0	0.3	1.5	0.005, 0.01	0, 50	0, 50	0, 20	0, 40	0, 40	0, 10
15	$3.14-18.85$	1200	1000	900	0	CV	10^{-6}	10^{-4}	0	0.15	0.2	0.05	0	0	0	0	0	0
16	$0.6283-6.283$	1200	1000	920	0	0.015	10^{-6}	CV	0	0.5	100	$0.001-0.005$	0	0	0	0	0	0
17, 18	$0.01-10$	1200	1030	850	0, 1.2	0.015	10^{-6}	10^{-4}	$0, 15\times10^{-6}$	0.5	10^0-10^4	0	0	0	0	0	0	0
19	$0.01-10$	1200	1030	850	0, 1.2	0.015	10^{-6}	10^{-4}	$0, 15\times10^{-6}$	0.5	$5-5000$	$0.002-0.010$	0	0	0	0	0	0

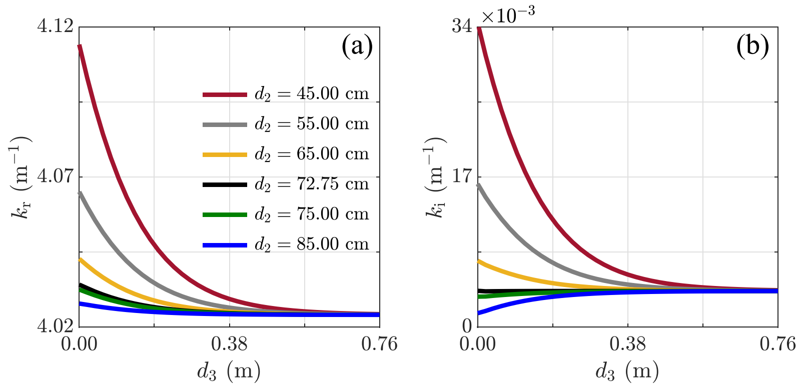

FIG. 6. The (a) wave number, k_r, and (b) spatial attenuation rate, k_i, as functions of the oil layer's depth, d_3, for different values of water layer depth, d_2. Wave frequency is $\omega = 1$ Hz and mud layer depth is $d_1 = 15$ cm. Numerical values of parameters used to obtain results are included in Table IV.

A. Influence of oil layer on wave attenuation

Here, we are interested in finding how the attenuation rate (k_i) changes as the depth of the oil layer (d_3) increases, for various sets of values of $\{d_1, d_2, \nu_3, \omega\}$. To begin with, Fig. 6 presents k_r and k_i as functions of d_3 for various values of d_2 (water layer depth). Interestingly, when the depth of water layer is less than a threshold value, $d_{2c} \approx 72.75$ cm, the attenuation rate k_i decreases as d_3 increases. For $d_2 = d_{2c}$, the attenuation rate k_i remains unaffected when d_3 changes; whereas when $d_2 > d_{2c}$, the attenuation rate k_i increases as d_3 increases. These results clearly show that a thicker oil layer does not necessarily imply a larger attenuation rate.

For a fixed value of d_3 in Fig. 6(b), we observe that k_i increases monotonically as d_2 decreases, indicating that for the conditions considered herein, a thicker water layer leads to a lower attenuation rate. This result is consistent with those from previous studies [66], demonstrating that wave damping rates are higher in shallow water than in deep water. Here $k_r \sim 4$ m^{-1} [see Fig. 6(a)], so it turns out that (i) $k_r d_2 \sim 1.8$ when $d_2 = 45$ cm (brown curves in Fig. 6); (ii) $k_r d_2 \sim 2.9$ when $d_2 = 72.75$ cm (black curves in Fig. 6); (iii) $k_r d_2 \sim 3.4$ when $d_2 = 85$ cm (blue curves in Fig. 6). Case (ii) represents the onset of the deep-water regime, so it is likely a reason why variations in the oil layer's depth (d_3) do not have a significant impact on the attenuation rate when $d_2 = 72.75$ cm. In case (iii), which clearly falls within the deep-water regime, there is a slight increase in the attenuation rate as the oil-layer thickness increases from zero; this is likely due to the change in dynamics of the system when d_3 increases from zero ($d_3 \to 0$ represents a monolayer of oil) to some finite value (which represents a thin oil layer). Though a monolayer of oil can significantly change the conditions at the boundary, it does not have its own velocity field. On the other hand, a thin layer of oil will have its own velocity field and boundary layer, and dissipation within this boundary layer could lead to an increase in the attenuation rate.

In Fig. 7, we present k_r and k_i as functions of d_3, for $d_2 = d_{2c}$ and various values of d_1. For fixed values of d_2 and d_3, we observe from Fig. 7(b) that k_i increases as d_1 increases from 2.5 cm to 15 cm, reaches a maximum, and then decreases as d_1 increases further from 15 cm to 75 cm, indicating that k_i is a nonmonotonic function of d_1. When $d_1 = 15$ cm, k_i remains unchanged as d_3 changes [see the black curve in Fig. 7(b); this is same as the black curve in Fig. 6(b)]. For $d_1 > 65$ cm, a change in d_1 does not lead to a corresponding change in k_i [note that the red solid curve and blue dashed-dotted curve in Fig. 7(b) are identical].

One notable observation is that the wave number (k_r) remains relatively unchanged in both Figs. 6(a) and 7(a), with numerical values varying within 10% of 4 m^{-1}. This result clearly indicates that variations in fluid layer depths have negligible effects on the wave number, whereas they cause substantial changes in the attenuation rates. In Fig. 7(b), k_i increases as d_3 increases (for all values

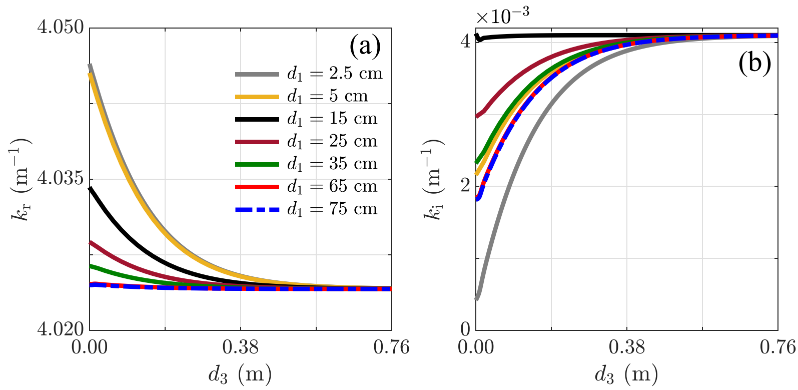

FIG. 7. The (a) wave number, k_r, and (b) spatial attenuation rate, k_i, as functions of the oil layer's depth, d_3, for different values of mud layer depth, d_1. Wave frequency is $\omega = 1$ Hz and water layer depth is $d_2 = 72.75$ cm. Numerical values of parameters used to obtain results are included in Table IV.

of d_1 and for $d_2 = 72.75$ cm), because $k_r d_2 \sim 3$, which indicates that the water layer is deep, for which the attenuation rate is expected to increase as the thickness of oil layer increases (as in Fig. 6(b) for $d_2 > d_{2c}$). In Fig. 7(b), k_i exhibits a nonmonotonic variation with d_1; this is possibly because the values of $k_r d_1$ fall within the range of $0.1 < k_r d_1 < 3$ for the values of d_1 considered here. This indicates that the mud layer exhibits a wide range of depths, spanning shallow, intermediate, and deep regimes for the data in Fig. 7(b). According to the results in Table III, nonmonotonic behavior can be expected when $k_r d_j$ transitions across unity, from shallow to deep regimes or vice-versa (see Sec. IV F for more discussion). Additionally, the thickness of the boundary layer in mud is $\delta_1 = 0.069$ m; so here the maximum attenuation rate seems to occur when $d_1/\delta_1 \sim 2$, consistent with the results in Table III.

Figure 8 presents k_i as a function of d_3 for various values of oil viscosity, ν_3. For large values of d_3, the attenuation rate k_i is independent of d_3, irrespective of the value of ν_3. For small values of d_3 (such that $k_r d_3 \lesssim 1$), the attenuation rate k_i increases as d_3 increases, only when $\nu_3 > \nu_{3c} \sim 8 \times 10^{-4}$ m^2/s. For values of $\nu_3 < \nu_{3c}$, k_i decreases as d_3 increases. This indicates that an increase in the attenuation rate is possible only when the effects of viscosity and fluid layer depth combine

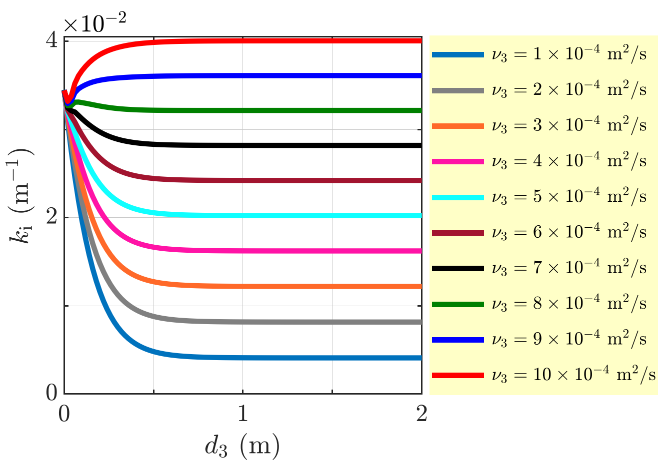

FIG. 8. The spatial attenuation rate, k_i, as a function of the oil layer's depth, d_3, for different values of oil viscosity, ν_3. Wave frequency is $\omega = 1$ Hz. Numerical values of parameters used to obtain results are included in Table IV. For these conditions, 4.03 m^{-1} $< k_r <$ 4.11 m^{-1}.

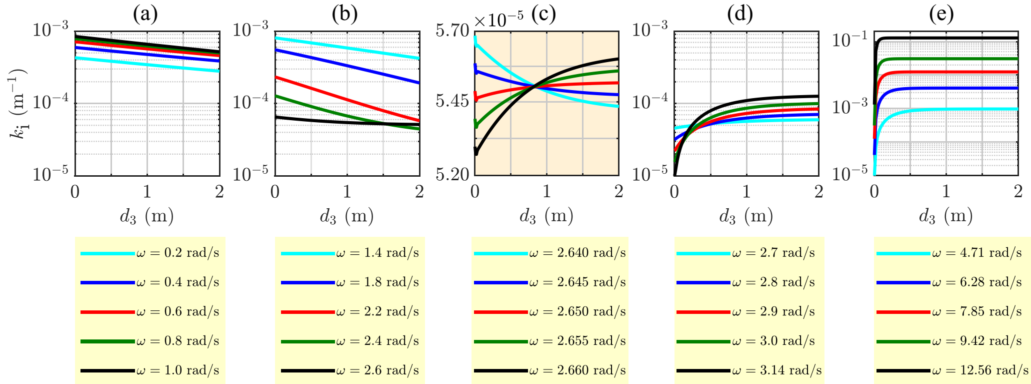

FIG. 9. The spatial attenuation rate, k_i, as a function of the oil layer's depth, d_3, for different values of wave frequency. Numerical values of parameters used to obtain results are included in Table IV.

effectively to enhance dissipation. These results corroborate the findings published in [7]. When d_3 is small enough that $d_3 \ll \delta_3 \ll k_\mathrm{r}^{-1}$ ($\delta_3 := \sqrt{2\nu_3/\omega}$ is the thickness of boundary layer within oil, which ranges from 0.6 cm to 1.8 cm here), the dynamics in the oil layer will be different—in this case, the oil layer is so thin that the velocity profile within it could turn out to be uniform or linear (with a small slope). As a result, the velocity gradients in the oil layer could be weak, and thus may not contribute much to the dissipation of energy.

Figure 9 presents the spatial attenuation rate (k_i) as a function of the thickness of oil layer (d_3) for various wave frequencies. When the frequency is less than a threshold value ($\sim$2.65 rad/s), k_i decreases as d_3 increases; beyond this frequency k_i increases as d_3 increases. For large frequencies and large depths of the oil layer, k_i becomes independent of d_3; this is because $k_\mathrm{r} d_3 \gg 1$ under such conditions, indicating that the oil layer is very deep. Figure 10 also presents the attenuation rate as a function of the depth of the oil layer for various frequencies, but the objective here is to observe how the depth of the water layer (d_2) changes the results. From Fig. 10, one can observe that there is a critical value of d_2 below which k_i decreases as d_3 increases; beyond this critical value, k_i increases

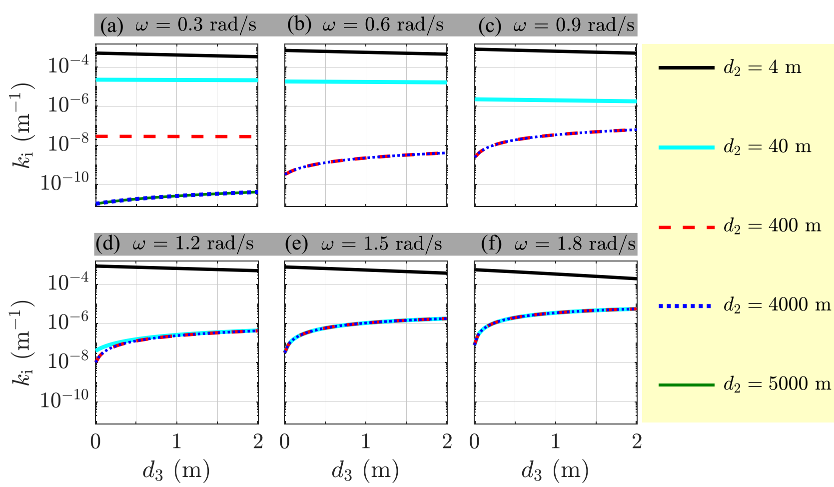

FIG. 10. The spatial attenuation rate, k_i, as a function of the oil layer's depth, d_3, for different values of wave frequency and water-layer depth, d_2. Numerical values of parameters used to obtain results are included in Table IV.

as d_3 increases. This critical value of d_2 lies between (i) 400 m and 4000 m for $\omega = 0.3$ rad/s; (ii) 40 m and 400 m for $\omega = 0.6$ rad/s and $\omega = 0.9$ rad/s; and (iii) 4 m and 40 m for $\omega = 1.2$ rad/s, $\omega = 1.5$ rad/s, and $\omega = 1.8$ rad/s [see Figs. 10(a)–10(f)]. When $\omega = 0.3$ rad/s, increasing the water layer depth, d_2, beyond 4000 m does not change the results [see Fig. 10(a)], whereas when $\omega = 1.5$ rad/s, increasing the water layer depth, d_2, beyond 40 m does not change the results [see Fig. 10(e)]. These results demonstrate the intricate relationships between several variables, reaffirming the fact that such detailed studies are necessary to determine the dominant factor in various situations and/or regimes.

B. Influence of mud layer on wave attenuation

To understand how wave attenuation rates are affected by variations in the depth of the mud layer, we used our model to obtain k_i as a function of d_1 for various values of the frequency; these results are presented in Fig. 11. Clearly, the attenuation rate exhibits nonmonotonic behavior with respect to the mud-layer depth, reaching a maximum (of magnitude k_i^*) at an intermediate depth, d_1^* (numerical values are recorded in Table V). To analyze the data in Table V, we present them in the form of graphs in Fig. 12. Figure 12(a) shows that k_i^* is a nonmonotonic function of d_1^*. However, when we nondimensionalize these variables using the inverse of wave number as the length scale, we observe that $\hat{k} := k_\mathrm{i}^*/k_\mathrm{r}^*$ becomes a monotonic function of $\hat{d}_1 := d_1^* k_\mathrm{r}^*$ [Fig. 12(b)]. To obtain an empirical equation that relates k_i^* and d_1^*, we take their logarithms and present the data in Fig. 12(c). It turns out that $\ln[\hat{k}] = -6.651 \exp(0.2534 \ln[\hat{d}_1]) - 499.8 \exp(4.261 \ln[\hat{d}_1])$, which is obtained (using MATLAB) by applying the Levenberg-Marquardt algorithm to the data. Finally, Fig. 12(d) shows that d_1^* varies linearly with δ_1, with a slope of approximately 1.1.

As shown in Fig. 11(b), Table V, and Fig. 12(d), the attenuation rate is maximized when d_1/δ_1 is (consistently) 10% more than unity. We observe that $0.01 \lesssim \hat{d}_1 := k_\mathrm{r}^* d_1^* \lesssim 0.2$ in Table V, indicating that the maximum attenuation rates occur when the mud layer is shallow. Combining these conditions, we can generalize that for the conditions and parameter ranges considered in Fig. 11(b), Table V, and Fig. 12(d), the maximum attenuation rates occur when $k_\mathrm{r}^{-1} \gg d_1 \sim 1.1\delta_1$. This criterion indicates that, for the attenuation rate to be maximized, the mud layer should be shallow, but its depth should exceed the thickness of the boundary layer. Since the mud-layer depth

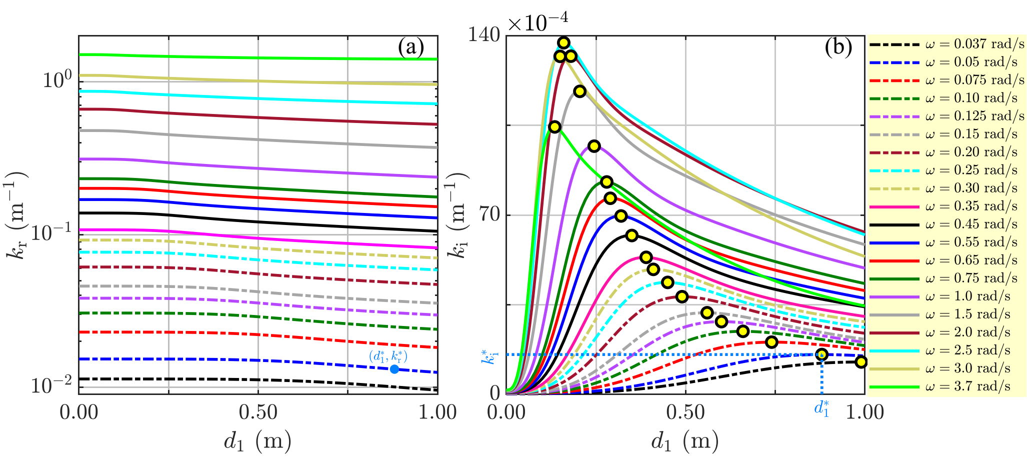

FIG. 11. The (a) wave number, k_r, and (b) spatial attenuation rate, k_i, as functions of the mud layer's depth, d_1, for different values of wave frequency. Numerical values of parameters used to obtain results are included in Table IV. The solid yellow circles with black borders in panel (b) indicate the peaks in the curves, with coordinates (d_1^*, k_i^*). The coordinates in panel (a) corresponding to the peak in panel (b) are (d_1^*, k_r^*). Here, these two sets of coordinates are specifically shown for $\omega = 0.05$ rad/s. The values of d_1^*, k_i^*, and k_r^* for each frequency are presented in Table V.

TABLE V. Data for the maximum attenuation rates in Fig. 11. Here k_i^* is the maximum attenuation rate obtained for each frequency; d_1^* and k_r^* are the mud-layer thickness and wave number corresponding to this maximum attenuation rate. For each frequency, the entire range of values taken by the wave number, k_r, is given in column 3. The boundary layer thicknesses are calculated using $\delta_j := \sqrt{2\nu_j/\omega}$. Data in this table are graphed in Fig. 12.

No.	ω (rad/s)	k_r (m^{-1})	k_r^* (m^{-1})	k_i^* (m^{-1})	d_1^* (m)	$\hat{k} = k_i^*/k_r^*$	$\hat{d}_1 = k_r^* d_1^*$	$\ln[\hat{k}]$	$\ln[\hat{d}_1]$	$1/k_r^*$ (m)	δ_1 (m)	δ_2 (m)	δ_3 (m)
1	0.037	0.00958–0.0113	0.00962	0.00126	0.99	0.131	0.00952	−2.03	−4.65	104	0.900	0.00735	0.0735
2	0.05	0.0125–0.0153	0.0131	0.00155	0.88	0.118	0.0116	−2.14	−4.46	76.3	0.775	0.00632	0.0632
3	0.075	0.0182–0.0230	0.0201	0.00204	0.74	0.101	0.0149	−2.29	−4.21	49.8	0.632	0.00516	0.0516
4	0.1	0.0240–0.0306	0.0270	0.00246	0.66	0.0910	0.0178	−2.40	−4.03	37.0	0.548	0.00447	0.0447
5	0.125	0.0297–0.0383	0.0341	0.00284	0.60	0.0833	0.0205	−2.49	−3.89	29.3	0.490	0.00400	0.0400
6	0.15	0.0355–0.0460	0.0411	0.00319	0.56	0.0775	0.0230	−2.56	−3.77	24.3	0.447	0.00365	0.0365
7	0.2	0.0471–0.0613	0.0555	0.00381	0.49	0.0686	0.0272	−2.68	−3.61	18.0	0.387	0.00316	0.0316
8	0.25	0.0587–0.0766	0.0698	0.00437	0.45	0.0626	0.0314	−2.77	−3.46	14.3	0.346	0.00283	0.0283
9	0.3	0.0703–0.0920	0.0845	0.00488	0.41	0.0577	0.0346	−2.85	−3.36	11.8	0.316	0.00258	0.0258
10	0.35	0.0818–0.107	0.0988	0.00535	0.39	0.0541	0.0385	−2.92	−3.26	10.1	0.293	0.00239	0.0239
11	0.45	0.105–0.138	0.128	0.00620	0.35	0.0484	0.0448	−3.03	−3.11	7.81	0.258	0.00211	0.0211
12	0.55	0.129–0.169	0.158	0.00696	0.32	0.0441	0.0505	−3.12	−2.99	6.33	0.234	0.00191	0.0191
13	0.65	0.152–0.201	0.188	0.00765	0.29	0.0406	0.0546	−3.20	−2.91	5.32	0.215	0.00175	0.0175
14	0.75	0.176–0.232	0.218	0.00829	0.28	0.0380	0.0610	−3.27	−2.80	4.59	0.200	0.00163	0.0163
15	1	0.238–0.312	0.295	0.00969	0.25	0.0328	0.0724	−3.42	−2.63	3.39	0.173	0.00141	0.0141
16	1.5	0.371–0.479	0.459	0.0118	0.21	0.0258	0.0940	−3.66	−2.37	2.18	0.141	0.00115	0.0115
17	2	0.526–0.661	0.638	0.0132	0.18	0.0207	0.115	−3.88	−2.17	1.57	0.122	0.00100	0.0100
18	2.5	0.717–0.866	0.842	0.0137	0.16	0.0163	0.135	−4.12	−2.01	1.19	0.110	0.000894	0.00894
19	3	0.959–1.10	1.08	0.0132	0.15	0.0123	0.162	−4.40	−1.82	0.926	0.100	0.000816	0.00816
20	3.7	1.41–1.50	1.49	0.0104	0.14	0.00703	0.201	−4.96	−1.61	0.671	0.0900	0.000735	0.00735

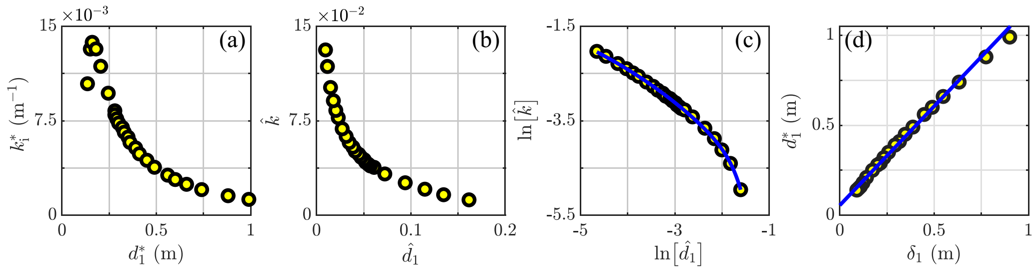

FIG. 12. Analysis of data presented in Table V. The solid blue curves in panels (c) and (d) have been fitted to the data and represent the following equations: $\ln[\hat{k}] = -6.651\exp(0.2534\ln[\hat{d}_1]) - 499.8\exp(4.261\ln[\hat{d}_1])$ and $d_1^* = 1.1006\delta_1 + 0.0553$, which were obtained using the Levenberg-Marquardt algorithm and linear least squares method, respectively.

is not significantly more than the boundary layer thickness here, the entire layer experiences high gradients in velocity, and consequently a significant fraction of fluid particles experience high rates of shear and rotation. When the layer is deep (and thus significantly thicker than the boundary layer), a significant fraction of fluid particles will lie outside the boundary layer and thus not experience high rates of shear and rotation. So, it is unlikely that the attenuation rates will be maximized when wave propagation is in the deep fluid regime.

C. Influence of interfacial tensions and elasticities on wave attenuation

So far, we assumed negligible interfacial tensions and elasticities. Here, we investigate how variations in these properties affect attenuation rates. To this end, we calculate the attenuation rates for different values of tension and elasticity and present them in Fig. 13. For the range of frequencies considered here, changes in interfacial tensions do not affect attenuation rates (in Fig. 13, compare panels in column A with those in column B, and panels in column C with those in column D),

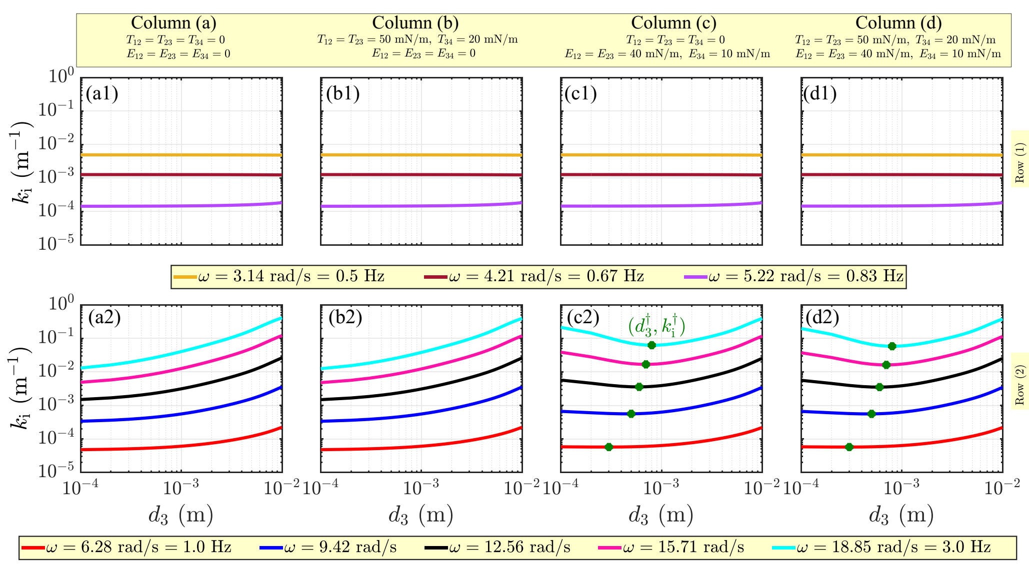

FIG. 13. The spatial attenuation rate, k_i, as a function of the oil layer's depth, d_3, for different values of interfacial tensions and elasticities. Numerical values of parameters used to obtain results are included in Table IV. The green dots in (c2) and (d2) represent the points of minimum attenuation rates, with coordinates $(d_3^\dagger, k_i^\dagger)$. The numerical values of these coordinates are presented in Table VI.

TABLE VI. Numerical values of the coordinates, $(d_3^\dagger, k_i^\dagger)$, corresponding to minimum attenuation rates in panels (c2) and (d2) of Fig. 13.

		Panel (c2) in Fig. 13		Panel (d2) in Fig. 13	
		$T_{12} = T_{23} = T_{34} = 0$		$T_{12} = T_{23} = 50$ mN/m, $T_{34} = 20$ mN/m	
		$E_{12} = E_{23} = 40$ mN/m, $E_{34} = 10$ mN/m		$E_{12} = E_{23} = 40$ mN/m, $E_{34} = 10$ mN/m	
No.	ω (rad/s)	$d_3^\dagger$ (m)	$k_i^\dagger$ (m^{-1})	$d_3^\dagger$ (m)	$k_i^\dagger$ (m^{-1})
1	6.28	0.0003	5.7472×10^{-5}	0.0003	5.7433×10^{-5}
2	9.42	0.0005	5.6206×10^{-4}	0.0005	5.5942×10^{-4}
3	12.56	0.0006	3.5750×10^{-3}	0.0006	3.5211×10^{-3}
4	15.71	0.0007	1.6771×10^{-2}	0.0007	1.6171×10^{-2}
5	18.85	0.0008	6.2617×10^{-2}	0.0008	5.8268×10^{-2}

because the wavelengths corresponding to these frequencies exceed typical capillary length scales. For high-frequency waves, we expect that variations in interfacial tensions will affect attenuation rates; one purpose of this section is to demonstrate that the current model can also be used to obtain results for waves of larger frequencies.

Comparing panels (a2) and (b2) with panels (c2) and (d2) respectively in Fig. 13 reveals that variations in interfacial elasticities significantly affect attenuation rates, especially for waves with frequencies above 1 Hz. The attenuation rate is minimized (to a value of $k_i^\dagger$) when the oil layer thickness reaches an intermediate value, $d_3^\dagger$ (see Table VI for numerical values). To explain this phenomenon, it is necessary to understand how surfactants work. When adsorbed onto an interface, surfactants render it elastic, imparting nonzero elasticity. Due to deformation of the interface caused by wave motion, the surfactant molecules become densely distributed at crests and sparsely distributed at troughs. The resulting gradients in concentration and interfacial tension cause the interface to undergo periodic cycles of compression and expansion in the direction of wave

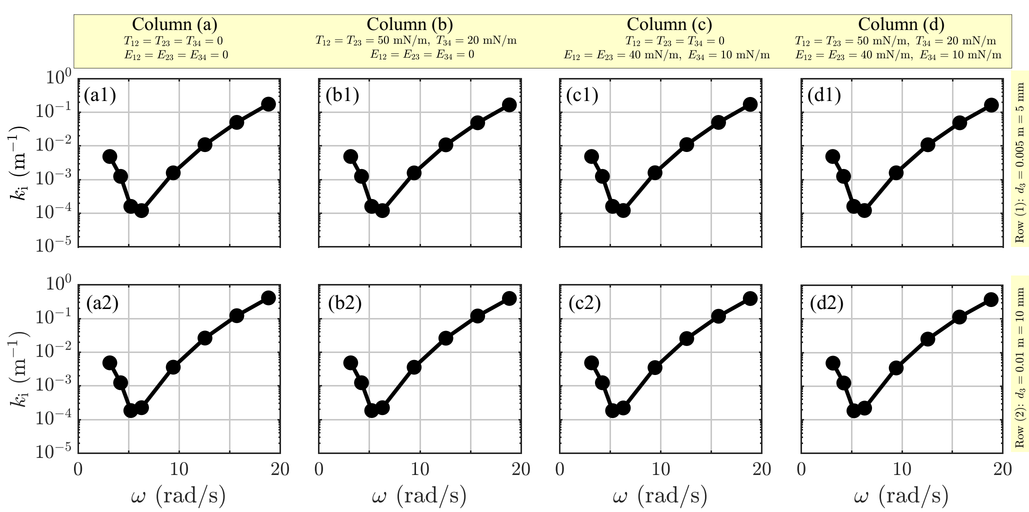

FIG. 14. The spatial attenuation rate, k_i, as a function of the wave frequency, for two different values of the oil-layer depth, $d_3 = 5$ mm (row 1) and $d_3 = 10$ mm (row 2). Numerical values of parameters used to obtain results are available in Table IV. Black dots represent tha data; solid black curves connect the dots.

propagation. These longitudinal oscillations affect the energy dissipation of gravity waves, leading to variable attenuation rates that can be maximized or minimized based on specific interfacial conditions and fluid layer depths. For more discussion on the interaction between gravity waves and these longitudinal oscillations, see [12,50,51,149].

Figure 14, which presents k_i as a function of ω for various cases, shows that k_i reaches a minimum at a critical frequency, $\omega_c \sim 5$ rad/s. For all cases in Fig. 14, the depth of the water layer is $d_2 = 1.5$ m; when $\omega < \omega_c$, it turns out that $k_r d_2 < 4.2$, so waves with these frequencies propagate on a fluid with shallow/intermediate depth. When $\omega > \omega_c$, wave propagation is on a deep fluid; so $\omega = \omega_c$ represents the onset of the deep-fluid regime. This could likely be the reason for minimization of the attenuation rate, but more detailed analyses are required to confirm the hypothesis. It is also worth noting that when $\omega = \omega_c$, the depth of the oil layer is on the same order as the thickness of the (oil) boundary layer, $\delta_3 := \sqrt{2\nu_3/\omega} = 6.3$ mm.

D. Influence of viscoelastic fluid behavior on wave attenuation

Here, we will investigate how the wave attenuation rates are affected when the (i) mud layer and (ii) oil layer are modeled as viscoelastic fluids. Figure 15 shows the results obtained by modeling the mud layer as a viscoelastic fluid using the Jeffrey and Maxwell equations, provided in (46). From this figure, we observe that results obtained using the viscoelastic models for mud are not significantly different from those obtained using the Newtonian fluid model, for the range of frequencies considered herein. The attenuation rate k_i exhibits a local maximum at $\omega = \omega_{c1} \approx 5.5$ rad/s and a local minimum at $\omega = \omega_{c2} \approx 11$ rad/s. Interestingly, the minimum occurs at a frequency which is twice the one at which the maximum occurs. Here $d_1 = 0.15$ m and $d_2 = 0.2$ m, so the frequency ω_{c1} (at which the maximum attenuation rate occurs) corresponds

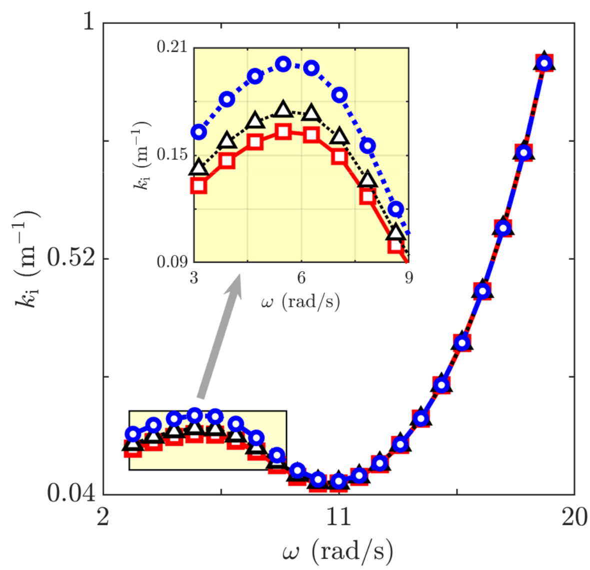

FIG. 15. Effects of viscoelastic mud on the attenuation rate. The red curve with squares represents the result obtained using a Newtonian fluid model for mud with $\nu_1 = 1.5 \times 10^{-2}$ m^2/s. The black curve with triangles represents the result obtained using the Jeffrey viscoelastic fluid model for mud with $\nu_1 := \nu_{1J}(1 + i\omega\lambda_2)/(1 + i\omega\lambda_1)$ and $\nu_{1J} = 0.0175$ m^2/s, $\lambda_1 = 1.07$ s, $\lambda_2 = 1$ s. The blue curve with circles represents the result obtained using the Maxwell viscoelastic model for mud with $\nu_1 := \nu_{1M}(1 + i\omega\lambda)/(1 + \omega^2\lambda^2)$ and $\nu_{1M} = 0.01667$ m^2/s, $\lambda = 0.0667$ s. Other numerical values used for various parameters are listed in Table IV.

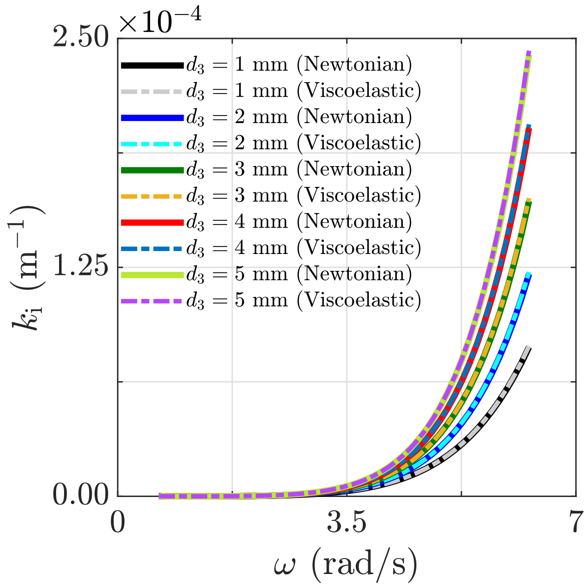

FIG. 16. Effects of viscoelastic oil on the attenuation rate. Solid curves represent the results obtained using a Newtonian fluid model for oil with $\nu_3 = 2.63 \times 10^{-4}$ m^2/s; dashed-dotted curves represent the results obtained using a viscoelastic fluid model for oil with $\nu_3 = \nu_{3r} + i\nu_{3i}$ and $\nu_{3r} = 2.63 \times 10^{-4}$ m^2/s, $\nu_{3i} = 4.5 \times 10^{-4}$ m^2/s. Other numerical values used for various parameters are presented in Table IV.

to $k_r d_1 \sim 0.54$, while the frequency ω_{c2} (at which the minimum attenuation rate occurs) corresponds to $k_r d_1 \sim 1.8$. Both conditions fall within the shallow fluid/intermediate depth regime. The boundary layer thicknesses in (Newtonian) mud, corresponding to these conditions, are $\delta_1 = \sqrt{2\nu_1/\omega_{c1}} \sim 0.074$ m and $\delta_1 = \sqrt{2\nu_1/\omega_{c2}} \sim 0.052$ m. So, the maximum attenuation rate occurs when $d_1/\delta_1 \sim 2$ (which is consistent with the result in Table III), while the minimum attenuation rate occurs when $d_1/\delta_1 \sim 2.9$. We observe that the maximization of attenuation rates was also reported by Xu and Guyenne [155], who employed a two-layer porous viscoelastic model to investigate wave attenuation in ice-covered seas, validating their results through comparisons with field data.

Figure 16 presents attenuation rates obtained by modeling the oil layer as a viscoelastic fluid with complex-valued viscosity. Within the parameter ranges and scales considered here, the results for viscoelastic oil show negligible deviation from those for Newtonian oil. We anticipate significant differences between results for viscoelastic and Newtonian oil at higher frequencies, particularly in the capillary wave regime. However, further studies are necessary to confirm this hypothesis.

E. Influence of air dynamics on wave attenuation

Here we investigate the impact of air dynamics on wave attenuation rates. To quantify this effect, we define the attenuation rate ratio

$$\alpha := \frac{k_i|_{\rho_4 \neq 0}}{k_i|_{\rho_4 = 0}}, \tag{47}$$

which compares the attenuation rate obtained by accounting for air dynamics with that obtained by neglecting them. A value of $\alpha = 1$ implies that air dynamics have no effect on wave attenuation, making them negligible. Values of α that significantly deviate from unity indicate that air dynamics will have a substantial impact on wave attenuation.

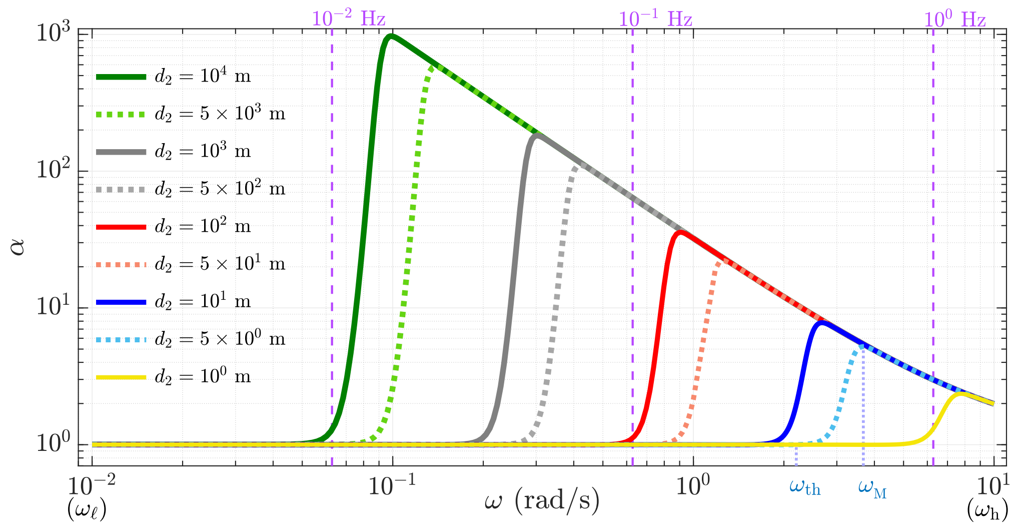

FIG. 17. The attenuation rate ratio, α, as a function of the wave frequency, ω, for various values of the water layer depth. Numerical values used for various parameters are presented in Table IV. Here ω_{th} is the threshold frequency at which α starts increasing from unity, and ω_{M} is the frequency at which α is maximum; these are marked for the blue dotted curve, which corresponds to $d_2 = 5$ m. Numerical values of ω_{th} and ω_{M} are presented in Table VII. The lowest and highest values of ω are represented by ω_ℓ and ω_{h}.

Figure 17 shows the attenuation rate ratio as a function of wave frequency for various depths of the water layer, d_2, ranging from 1 m to 10 km. One may observe that for each value of d_2, the attenuation rate ratio (i) stays constant at unity as the frequency increases from $\omega_\ell \sim 10^{-2}$ rad/s to an intermediate threshold value, ω_{th}, (ii) increases from unity to a maximum value, $\alpha_{\text{M}} := \alpha|_{\omega_{\text{M}}}$, as the frequency increases from ω_{th} to ω_{M} (which is the frequency at which α is maximized), and (iii) decreases from α_{M} as the frequency increases further from ω_{M} to $\omega_{\text{h}} \sim 10$ rad/s. Mathematically,

$$\frac{\mathrm{d}\alpha}{\mathrm{d}\omega} \text{ is } \begin{Bmatrix} \sim 0 & \text{for} & \omega_\ell < \omega \leqslant \omega_{\text{th}}, \\ > 0 & \text{for} & \omega_{\text{th}} < \omega < \omega_{\text{M}}, \\ = 0 & \text{for} & \omega = \omega_{\text{M}}, \\ < 0 & \text{for} & \omega_{\text{M}} < \omega \leqslant \omega_{\text{h}}. \end{Bmatrix} \tag{48}$$

Naturally, ω_{th} and ω_{M} are functions of d_2; their numerical values are presented in Table VII.

To analyze the data in Table VII and identify trends, we graph them in Fig. 18. One may identify clear trends in Table VII and Fig. 18: (i) a tenfold increase in d_2 is accompanied by (approximately) a threefold decrease in ω_{th} (ii) a tenfold increase in d_2 is accompanied by (approximately) a threefold decrease in ω_{M}, and (iii) a tenfold increase in d_2 is accompanied by (approximately) an n-fold increase in α_{M}, where $3 \lesssim n \lesssim 5$. Typically, the results in panels (a2), (b2), and (c2) of Fig. 18 indicate that $\omega_{\text{th}} \sim 1/\sqrt{d_2}$, $\omega_{\text{M}} \sim 1/\sqrt{d_2}$, and $\alpha_{\text{M}} \sim d_2^{2/3}$. The results in Fig. 17 and Table VII clearly demonstrate that air dynamics is an important factor that contributes to wave attenuation, especially for frequencies that exceed the threshold value, ω_{th}. Figure 18 shows the range of frequencies for which air dynamics plays a significant role in increasing attenuation rates, for each value of d_2. As d_2 increases, the frequency range where air dynamics become significant also increases. When the wave frequency is close to ω_{M}, the attenuation rate increases significantly if one accounts for air dynamics; in fact α is maximized when $\omega = \omega_{\text{M}}$. Remarkably, $\alpha \sim 10^3$ when $d_2 = 10$ km and $\omega = 0.1$ rad/s, which shows that neglecting air dynamics for waves in such situations will result in large errors in the estimation of attenuation rates. As a result, it is advised to

TABLE VII. Values of $\omega_{\rm th}$ and $\omega_{\rm M}$, and the corresponding values of α. Each row corresponds to a specific value of d_2. Data obtained from Fig. 17.

No.	d_2 (m)	$\omega_{\rm th}$ (rad/s)	$\alpha_{\rm th} = \alpha\vert_{\omega_{\rm th}}$	$\omega_{\rm M}$ (rad/s)	$\alpha_{\rm M} = \alpha\vert_{\omega_{\rm M}}$
1	1	4.515	1.0010	7.766	2.358
2	5	2.214	1.0010	3.678	5.212
3	10	1.588	1.0010	2.677	7.798
4	50	0.7202	1.0010	1.258	22.18
5	100	0.5125	1.0010	0.9053	35.74
6	500	0.2302	1.0010	0.4207	111.0
7	1000	0.1604	1.0010	0.3020	182.1
8	5000	0.0602	1.0010	0.1387	583.9
9	10000	0.02964	1.0019	0.09873	971.5

account for air dynamics while estimating the attenuation rates of waves propagating on deep water, especially when the frequencies are low. Table VIII shows the wave numbers corresponding to the data in Fig. 17, Table VII, and Fig. 18, and highlights that the cases considered herein range from extremely shallow depths with $k_{\rm r}d_2 \sim 10^{-3}$ to very large depths with $k_{\rm r}d_2 \sim 10^5$.

The data in Fig. 17, Table VII, and Fig. 18 are for $d_3 = 0$, so to investigate how variations in the thickness of the oil layer affect attenuation rates, we present results for $d_3 > 0$ in Fig. 19. When the water layer is relatively shallow [see Fig. 19(a)], changes in d_3 lead to noticeable changes in α, but only when wave frequencies are high. When the water layer is deep [see Fig. 19(d)], changes

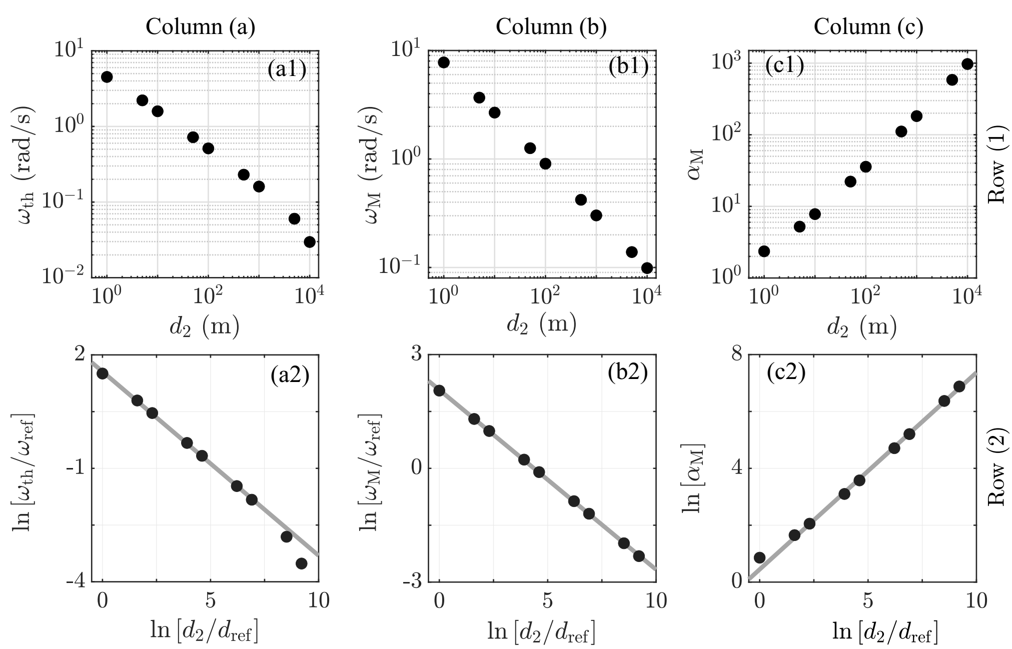

FIG. 18. The frequencies, $\omega_{\rm th}$, $\omega_{\rm M}$, and the maximum attenuation rate ratio, $\alpha_{\rm M}$, as functions of d_2. See Table VII for the data. Row 1 presents the data as they are, and row 2 presents the logarithms of these values. Here $\omega_{\rm ref} = 1$ rad/s and $d_{\rm ref} = 1$ m. The gray lines are linear curves fitted to the data and have the following equations. Panel (a2): $\ln[\omega_{\rm th}/\omega_{\rm ref}] = -0.4866\ \ln[d_2/d_{\rm ref}] + 1.5590$; panel (b2): $\ln[\omega_{\rm M}/\omega_{\rm ref}] = -0.4741\ \ln[d_2/d_{\rm ref}] + 2.0701$; panel (c2): $\ln[\alpha_{\rm M}] = 0.6922\ \ln[d_2/d_{\rm ref}] + 0.4469$.

TABLE VIII. Wave numbers corresponding to the data in Fig. 17, Table VII, and Fig. 18. Each case corresponds to a water layer of shallow, intermediate, or large depth.

No.	ω (rad/s)	d_2 (m)	k_r (m^{-1})	$2\pi/k_r$ (m)	$k_r d_2$	Classification
1	10^{-2}	10^0	3.1987×10^{-3}	1.9643×10^3	3.1987×10^{-3}	Shallow
		10^1	1.0099×10^{-3}	6.2217×10^3	1.0099×10^{-2}	Shallow
		10^2	3.1934×10^{-4}	1.9675×10^4	3.1934×10^{-2}	Shallow
		10^3	1.0114×10^{-4}	6.2123×10^4	1.0114×10^{-1}	Shallow
		10^4	3.2486×10^{-5}	1.9341×10^5	3.2486×10^{-1}	Intermediate
2	10^{-1}	10^0	3.0059×10^{-2}	2.0903×10^2	3.0059×10^{-2}	Shallow
		10^1	1.0058×10^{-2}	6.2469×10^2	1.0058×10^{-1}	Shallow
		10^2	3.2469×10^{-3}	1.9351×10^3	3.2469×10^{-1}	Intermediate
		10^3	1.2166×10^{-3}	5.1645×10^3	1.2166×10^0	Intermediate
		10^4	1.0206×10^{-3}	6.1567×10^3	1.0206×10^1	Deep
3	10^0	10^0	2.7890×10^{-1}	2.2529×10^1	2.7890×10^{-1}	Shallow
		10^1	1.2040×10^{-1}	5.2186×10^1	1.2040×10^0	Intermediate
		10^2	1.0206×10^{-1}	6.1566×10^1	1.0206×10^1	Deep
		10^3	1.0206×10^{-1}	6.1566×10^1	1.0206×10^2	Deep
		10^4	1.0206×10^{-1}	6.1566×10^1	1.0206×10^3	Deep
4	10^1	10^0	1.0206×10^1	6.1564×10^{-2}	1.0206×10^1	Deep
		10^1	1.0206×10^1	6.1564×10^{-2}	1.0206×10^2	Deep
		10^2	1.0206×10^1	6.1564×10^{-2}	1.0206×10^3	Deep
		10^3	1.0206×10^1	6.1564×10^{-2}	1.0206×10^4	Deep
		10^4	1.0206×10^1	6.1564×10^{-2}	1.0206×10^5	Deep

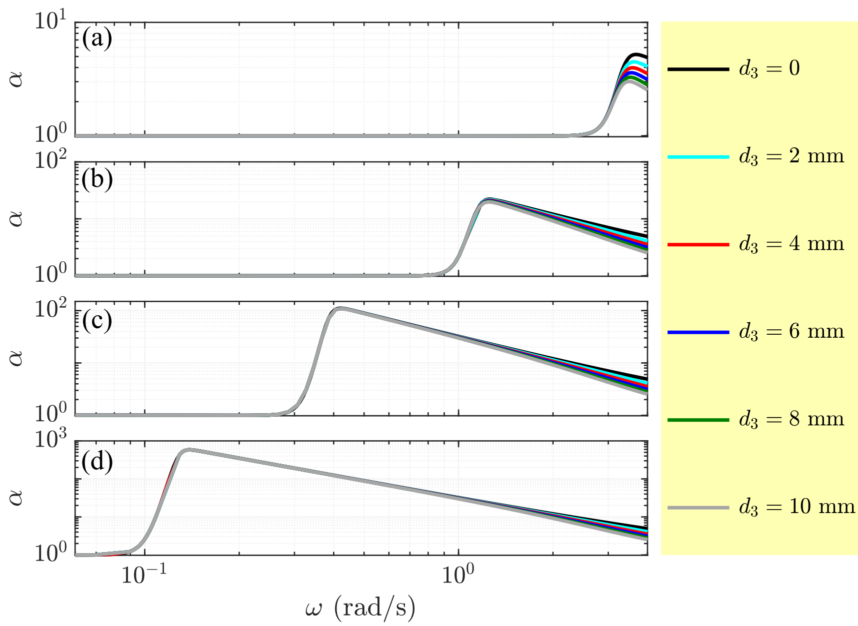

FIG. 19. Effect of oil layer thickness, d_3, on the attenuation rate ratio, α. Panels (a)–(d) correspond to four different values of the water layer depth: $d_2 = 5$ m, $d_2 = 50$ m, $d_2 = 500$ m, and $d_2 = 5000$ m. Other numerical values used for various parameters are listed in Table IV.

in d_3 do not lead to significant changes in α, reaffirming the fact that for waves of low frequencies propagating on deep water, the dominant factor contributing to their attenuation will be the dynamics in air.

F. Discussion

This problem involves a multitude of parameters: $\{\rho_1, \rho_2, \rho_3, \rho_4, \nu_1, \nu_2, \nu_3, \nu_4, T_{12}, T_{23}, T_{34}, E_{12}, E_{23}, E_{34}, d_1, d_2, d_3\}$; and the complex interactions among them make it challenging to understand the dynamics. Several factors could compete to increase or decrease the attenuation rate in various cases, necessitating a detailed analysis to identify the dominant one in each case. For the sake of argument, we will neglect the fourth layer (which amounts to replacing air with a vacuum) in the multilayered fluid system shown in Fig. 1, and replace the remaining three fluid layers with a single homogeneous fluid layer of depth $h = d_1 + d_2 + d_3$ and effective viscosity ν. For consistency, the properties of this single homogeneous fluid layer should effectively capture the dynamics of the three-fluid combination in the original multilayered system. To that end, the effective viscosity, ν, should be an appropriate average of ν_1, ν_2, and ν_3. Traditional techniques such as volume averaging may not yield desired results for the effective viscosity. Ideally, energy dissipation (due to effective viscosity) in the homogeneous single-layer fluid system should match the total dissipation in the original three-layered system (neglecting air in Fig. 1). Given the complexity of this problem, it is unlikely that a single model for the effective viscosity will work in all cases, rendering its estimation a significant challenge. However, results relevant to the homogeneous single-fluid system can serve as a reference and contribute to our understanding of the dynamics of a multilayered system.

Here, we analyze the simplified system with a single homogeneous fluid layer of depth h and kinematic viscosity ν. The attenuation rate for waves in this single-layer fluid system is (see Ref. [9]—their results are for waves propagating in a tank of finite width; we present results here for the limiting case of infinite width)

$$k_{\mathrm{i}} = \sqrt{\frac{2\nu}{\omega}}\left\{\frac{k_{\mathrm{r}}^2}{2k_{\mathrm{r}}h + \sinh(2k_{\mathrm{r}}h)}\right\}, \tag{49a}$$

$$= \sqrt{\frac{2\nu}{g^{1/2}}}\left\{\frac{k_{\mathrm{r}}^{7/4}}{[\tanh(k_{\mathrm{r}}h)]^{1/4}[2k_{\mathrm{r}}h + \sinh(2k_{\mathrm{r}}h)]}\right\}, \tag{49b}$$

where $k_{\mathrm{r}} > 0$ is the wave number, and we have used the dispersion relation, $\omega^2 = gk_{\mathrm{r}}\tanh(k_{\mathrm{r}}h)$, to obtain (49b) from (49a). It is easy to verify that k_{i} [in (49b)] is maximized when $k_{\mathrm{r}}h \sim 0.933$ (irrespective of the value of h), indicating that the maximum attenuation rate is obtained when waves propagate on the surface of a fluid layer of intermediate depth that is neither shallow nor deep.

Realizing that $\delta := \sqrt{2\nu/\omega}$ is the boundary layer thickness, one may rewrite (49b) as

$$k_{\mathrm{i}} = \frac{\delta k_{\mathrm{r}}^2}{2k_{\mathrm{r}}h + \sinh(2k_{\mathrm{r}}h)}, \tag{50a}$$

and then group appropriate terms to obtain the nondimensional form,

$$[k_{\mathrm{i}}h]\left[\frac{h}{\delta}\right] = \frac{(k_{\mathrm{r}}h)^2}{2k_{\mathrm{r}}h + \sinh(2k_{\mathrm{r}}h)} =: \beta, \tag{50b}$$

which is maximized when $k_{\mathrm{r}}h \sim 1.1997$ (see Fig. 20). Incidentally, the nondimensional group velocity, defined as

$$\hat{c}_{\mathrm{g}} := \frac{2\omega}{g}c_{\mathrm{g}} = \tanh(k_{\mathrm{r}}h) + k_{\mathrm{r}}h\,\mathrm{sech}^2(k_{\mathrm{r}}h), \tag{51}$$

also happens to be maximum when $k_{\mathrm{r}}h \sim 1.1997$ (see Fig. 20). Here $c_{\mathrm{g}} = \partial\omega/\partial k_{\mathrm{r}}$ is the dimensional group velocity, and can be obtained from the dispersion relation, $\omega^2 = gk_{\mathrm{r}}\tanh(k_{\mathrm{r}}h)$. Figure 20

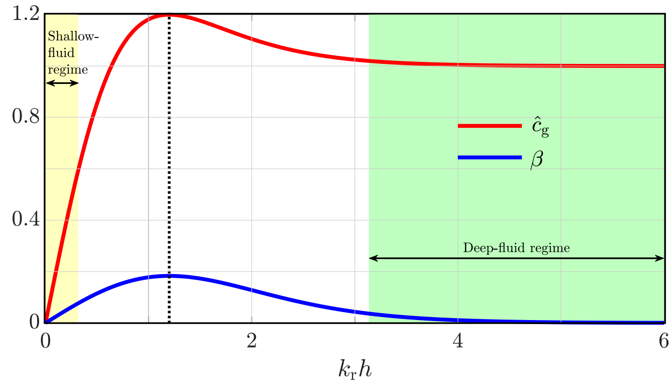

FIG. 20. Graphs of β and $\hat{c}_g$. See (50b) and (51) for the equations. The vertical black dotted line represents $k_r h = 1.1997$. The yellow and green shaded regions represent the shallow-fluid and deep-fluid regimes.

demonstrates that there is a strong correlation between the nondimensional parameter β (which is related to the attenuation rate, k_i) and the nondimensional group velocity. Indeed, wave energy is transported at the group velocity, so the result in Fig. 20, that the condition which maximizes β also maximizes $\hat{c}_g$, may not be so surprising after all. This condition, $k_r h \sim 1.1997$, falls within the intermediate-depth regime which separates the shallow-fluid and deep-fluid regimes (see Fig. 20). One must note that the values of $k_r h$ that maximize k_i and β are not same—in fact, they are $\sim 7\%$ less than and $\sim 20\%$ more than unity. These results apply to waves in a single-layer fluid system; the results for a two-layer fluid system may be different. Due to complexities in the multilayered fluid system, it is unlikely that the group velocity for this wave system will have a simple and explicit functional form such as in (51); but the analysis here clearly underlines the involvement of group velocity in the variation of wave attenuation rate. In fact, it is worth noting that the attenuation rates for waves in a system comprising water and mud layers (with comparable depths) are maximum when $k_r d_1 \sim O(1)$ (see Fig. 5 and Table III), which is in line with the results for a single-layer fluid system obtained here.

If the depth, h, is large compared to the wavelength ($k_r h \gg 1$, region shaded in green in Fig. 20), then the waves do not feel the bottom, and friction at the floor is too weak to contribute to the attenuation of surface waves. In this regime, particle trajectories are circular, with diameters decreasing exponentially with depth. In contrast, for small depths ($k_r h \ll 1$, region shaded in yellow in Fig. 20), particle trajectories become elliptical due to significant frictional effects, with the length of major axis remaining almost unchanged, but the length of minor axis decreasing with depth. For very small depths ($h < \delta$), the velocity profile within the fluid layer may be a linear function with a gentle slope, resulting in weak gradients and consequently, weak dissipation. This regime is prone to wave breaking, which is outside the scope of this study. Deep fluid waves, being dispersive, and shallow fluid waves, being nondispersive, differ in their group velocities, resulting in varying rates of wave energy transport in each regime. The nondimensional group velocity reaches its maximum value of ~ 1.2 at a point within the transitional wave regime (intermediate region with white background in Fig. 20), where the fluid depth is comparable to wavelength. As discussed in the preceding paragraph, maximum wave dissipation occurs at an optimal value of $k_r h$ which also falls within the transitional wave regime, which uniquely combines characteristics of deep-fluid and shallow-fluid regimes, featuring elliptical particle trajectories with both major axis and minor axis lengths decreasing with depth. Indeed, studies have demonstrated that wave dissipation differs in magnitude between shallow-fluid and deep-fluid regimes, with attenuation rates transitioning from $O(\sqrt{\nu})$ in the former to $O(\nu)$ in the latter (see [66]).

To gain deeper insight into wave dissipation in a multilayered fluid system, we will assume that the velocity field can be decomposed into two components: a potential-flow part (represented by a potential function) and a rotational-flow part (represented by a stream function). It can be verified that the amplitudes of the stream function are proportional to the term $\exp(|m_j|z)$. The parameter m_j, which is tagged to the rotational-flow part of the velocity field, contains information regarding the rate at which particle velocities decay in the direction perpendicular to wave propagation. Alternately, $|m_j|^{-1}$ can be regarded as a "penetration depth," defined as the vertical e-folding length scale beyond which rotational motions become weak. By decomposing the velocity vector in Navier-Stokes equation into potential-flow and rotational-flow components, it can be shown that wave dissipation is due to the rotational-flow component, which in turn depends on the penetration depth. A lower value of $|m_j|$ indicates that rotational effects penetrate a larger volume of the jth layer, with a greater number of fluid particles undergoing vortical motions. Recasting (24) as

$$\frac{m_j}{k} = \pm\left[1 - \frac{2\mathrm{i}}{(k\delta_j)^2}\right]^{1/2}, \tag{52}$$

where $\delta_j := \sqrt{2\nu_j/\omega}$ is the thickness of the boundary layer within the jth fluid layer, we realize that $|m_j| \geqslant |k|$. In most cases, it is expected that $|k|\delta_j \ll 1$, so (52) implies that $|m_j| \gg |k|$ and that the penetration depth is on the order of the boundary layer thickness, $|m_j|^{-1} \sim \delta_j$.

We anticipate that the wave attenuation rate will reach its maximum when rotational effects pervade the majority of the fluid volume, and when velocity gradients—comprising both strain rates and rotation rates—are substantial. Several factors contribute to wave attenuation, including viscous shear, dissipation due to finite depth effects, and energy removal due to compression-expansion oscillations of an elastic interface. Ultimately, the combination of factors that maximizes the velocity gradients will likely lead to the maximum attenuation rate in each case. For example, in the case for which results are presented in Fig. 5 and Table III, the attenuation rates are maximized when $k_\mathrm{r}d_1 \sim 1$ and $d_1/\delta_1 \sim 2$, while in the case for which results are presented in Fig. 11 and Table V, the attenuation rates are maximized when $d_1/\delta_1 \sim 1.1$. In contrast, in the case for which results are presented in Fig. 14, conditions cause minimization of dissipation rates. The ratio d_j/δ_j quantifies the overlap between the upper and lower boundary layers within the jth fluid layer. Values of d_j/δ_j on the order of 1–2 indicate substantial to moderate overlap, implying that rotational motions prevail throughout or in most part of the fluid layer. This could likely be a reason why attenuation rates are maximized when $1 \lesssim d_j/\delta_j \lesssim 2$. The fluid layer is thin if $d_j/\delta_j < 1$, and it is unlikely that the velocity gradients are strong in this case.

We understand that several factors such as wave breaking have been neglected in our model. Indeed, the experiments of Van Dorn [9] demonstrate that many "waves were markedly asymmetric and on the verge of breaking" in the shallowest water layer they considered, and this breaking seems to be a significant mechanism of energy dissipation. As discussed in Sec. I C, our model has limitations—factors such as the formation of microemulsion layers, evaporation, biodegradation, weathering, and turbulence have not been accounted for. Nevertheless, this model provides a theoretical framework for estimating attenuation rates for a wide range of depths, fluid properties, and frequencies, and is thus suitable for various applications. Moreover, this study provides a foundational basis for future investigations into the complex dynamics of multilayered fluid systems.

V. SUMMARY

In this work, we investigated the attenuation rates of waves in a stepwise-stratified multilayered fluid configuration that mimics the atmosphere-ocean system. The uniqueness of this work is the development of a theoretical model for the dispersion relation, which may then be solved either numerically or analytically depending on the complexity of the problem. Our review of relevant literature revealed that research on wave attenuation in multilayered fluid systems is relatively scarce; this motivated us to undertake this study. The salient features of this work include the inclusion of a bottom layer ($j = 1$) which accounts for a muddy seafloor; an interfacial layer of fluid ($j = 3$) between air and water, which could be composed of oil from spills, biogeneic films, plankton, dead decaying matter, by-products formed due to burning of spilled oil, and other constituents of the sea surface microlayer; and elastic interfaces.

We began by spelling out the details of the boundary value problem comprising the governing equations and boundary conditions. The model we developed is applicable to linear, monochromatic, unidirectional, freely propagating waves. The flow is laminar, two-dimensional, incompressible, and the layer depths are uniform when there is no flow. Fluid properties are uniform and variations due to thermal stratification are not taken into account. Assuming appropriate waveforms for velocity fields, pressure fields, and displacement fields, we carried out a rigorous mathematical analysis to obtain expressions for the elements of a 14×14 matrix, whose determinant, when equated to zero, yields the dispersion relation. We also outlined the solution procedure to obtain the wave attenuation rates numerically using MATLAB.

Thereafter, we proceeded to validate the model by comparing the results obtained (for a few cases of interest) with previously published theoretical results and experimental data. After establishing the authenticity of the model and realizing that this problem involves an extensive set of variables, we set out to perform detailed parametric studies to investigate the effects of different parameters on wave attenuation. We investigated dissipation trends in different regimes, and observed that attenuation rates are maximized or minimized under specific conditions, which prompted us to examine the underlying causes. Finally, we discussed our results, outlining our understanding of wave attenuation rate behaviors and their relations to group velocities and penetration depths, and proposed possible reasons that can explain the observed trends. The major conclusions of this work are listed below.

(1) This model is capable of predicting the spatial attenuation rates of gravity waves that are consistent with experimental measurements and results from other studies.

(2) This model can be used to obtain attenuation rates of gravity waves in a multilayered fluid system, for a wide range of cases, without any restrictions on the frequency, layer depths, and fluid/interface properties.

(3) This model accounts for a finitely thick interfacial layer of fluid (typically oil) between air and water, and another finitely thick layer of fluid (typically fluidized mud) below water, and yields results which reveal that the dynamics within both these layers significantly affect attenuation rates, especially for shallow fluid waves and transitional waves.

(4) The attenuation rates of waves propagating in a water-mud system are maximized when mud layer thickness is on the order of the wavelength ($k_r d_1 \sim 1$) and when the mud layer's depth is approximately two to three times the boundary layer thickness ($2 < d_1/\delta_1 < 3$), for the parameter ranges considered herein.

(5) The attenuation rates of gravity waves in an oil-water-mud system are significantly affected due to changes in the oil layer's thickness and viscosity, and the rate of increase/decrease in the attenuation rate with oil-layer depth depends on the value of water layer's depth.

(6) The attenuation rates of gravity waves with frequencies in the range of 0.037 Hz to 3.7 Hz, propagating in an oil-water-mud system, are maximized when the thickness of the mud layer is approximately 10% more than the boundary layer thickness, irrespective of the frequency.

(7) The attenuation rates of gravity waves in an oil-water-mud system are significantly affected by variations in interfacial elasticities, which are nonzero if the interfaces are contaminated with surfactants.

(8) The attenuation rates of waves in an oil-water-mud system are not significantly affected if either the oil layer or the mud layer is modeled as a viscoelastic fluid (with a complex-valued viscosity), for the parameter ranges considered herein.

(9) The attenuation rates of gravity waves in an air-oil-water-mud system are significantly impacted by air dynamics, especially when frequencies are low and the water layer is deep, with the attenuation rate obtained by accounting for air dynamics being three orders of magnitude greater than the one obtained by neglecting them for one particular case.

(10) The frequency at which the attenuation rate ratio is maximized varies as the inverse root of the water layer depth ($\omega_M \sim 1/\sqrt{d_2}$), and the corresponding maximum attenuation rate ratio varies

as the two-third power of the water layer depth ($\alpha_{\mathrm{M}} \sim d_2^{2/3}$), clearly indicating that air dynamics cannot be neglected in these cases.

Although our model has limitations, as outlined in Sec. I C, our results unequivocally demonstrate its significance and usefulness. Specifically, there are no restrictions on the numerical values that the model parameters can take, which showcases its versatility and applicability to a wide range of situations. The results produced here will be useful in a variety of applications including the estimation of thicknesses of oil films on the sea surface during remote sensing, modeling of interfacial phenomena, design of offshore structures, estimating sediment transport, and weather forecasting. Finally, we anticipate that our results will inspire and pave the way for future research in this area.

ACKNOWLEDGMENTS

This research was partially funded by the Science and Engineering Research Board (SERB), a statutory body under the Department of Science and Technology, Government of India, under Award No. SRG/2019/001513.

L.S.: Software, Formal Analysis, Investigation, Data Curation, Validation, Creating Figures and Tables, Writing—Review and Editing. G.K.R.: Conceptualization, Research Design and Methodology, Formal Analysis, Investigation, Validation, Visualization, Resources, Writing—Original Draft, Writing—Review and Editing, Supervision, Project Administration, Funding Acquisition.

DATA AVAILABILITY

The data supporting this study's findings are available within the article.

APPENDIX: ELEMENTS OF $\mathcal{A}$

The elements of the coefficient matrix $\mathcal{A}$ are the following:

$$\begin{aligned} \mathrm{a}_{1,1} &= \mathrm{a}_{1,5} = \mathrm{a}_{1,6} = \mathrm{a}_{1,7} = \mathrm{a}_{1,8} = \mathrm{a}_{1,9} = \mathrm{a}_{1,10} = \mathrm{a}_{1,11} = \mathrm{a}_{1,12} = \mathrm{a}_{1,13} = \mathrm{a}_{1,14} = \mathrm{a}_{2,2} = \mathrm{a}_{2,5} \\ &= \mathrm{a}_{2,6} = \mathrm{a}_{2,7} = \mathrm{a}_{2,8} = \mathrm{a}_{2,9} = \mathrm{a}_{2,10} = \mathrm{a}_{2,11} = \mathrm{a}_{2,12} = \mathrm{a}_{2,13} = \mathrm{a}_{2,14} = \mathrm{a}_{3,6} = \mathrm{a}_{3,9} = \mathrm{a}_{3,10} \\ &= \mathrm{a}_{3,11} = \mathrm{a}_{3,12} = \mathrm{a}_{3,13} = \mathrm{a}_{3,14} = \mathrm{a}_{4,5} = \mathrm{a}_{4,9} = \mathrm{a}_{4,10} = \mathrm{a}_{4,11} = \mathrm{a}_{4,12} = \mathrm{a}_{4,13} = \mathrm{a}_{4,14} = \mathrm{a}_{5,5} \\ &= \mathrm{a}_{5,9} = \mathrm{a}_{5,10} = \mathrm{a}_{5,11} = \mathrm{a}_{5,12} = \mathrm{a}_{5,13} = \mathrm{a}_{5,14} = \mathrm{a}_{6,6} = \mathrm{a}_{6,9} = \mathrm{a}_{6,10} = \mathrm{a}_{6,11} = \mathrm{a}_{6,12} = \mathrm{a}_{6,13} \\ &= \mathrm{a}_{6,14} = \mathrm{a}_{7,1} = \mathrm{a}_{7,2} = \mathrm{a}_{7,3} = \mathrm{a}_{7,4} = \mathrm{a}_{7,10} = \mathrm{a}_{7,13} = \mathrm{a}_{7,14} = \mathrm{a}_{8,1} = \mathrm{a}_{8,2} = \mathrm{a}_{8,3} = \mathrm{a}_{8,4} \\ &= \mathrm{a}_{8,9} = \mathrm{a}_{8,13} = \mathrm{a}_{8,14} = \mathrm{a}_{9,1} = \mathrm{a}_{9,2} = \mathrm{a}_{9,3} = \mathrm{a}_{9,4} = \mathrm{a}_{9,9} = \mathrm{a}_{9,13} = \mathrm{a}_{9,14} = \mathrm{a}_{10,1} = \mathrm{a}_{10,2} \\ &= \mathrm{a}_{10,3} = \mathrm{a}_{10,4} = \mathrm{a}_{10,10} = \mathrm{a}_{10,13} = \mathrm{a}_{10,14} = \mathrm{a}_{11,1} = \mathrm{a}_{11,2} = \mathrm{a}_{11,3} = \mathrm{a}_{11,4} = \mathrm{a}_{11,5} = \mathrm{a}_{11,6} \\ &= \mathrm{a}_{11,7} = \mathrm{a}_{11,8} = \mathrm{a}_{12,1} = \mathrm{a}_{12,2} = \mathrm{a}_{12,3} = \mathrm{a}_{12,4} = \mathrm{a}_{12,5} = \mathrm{a}_{12,6} = \mathrm{a}_{12,7} = \mathrm{a}_{12,8} = \mathrm{a}_{13,1} \\ &= \mathrm{a}_{13,2} = \mathrm{a}_{13,3} = \mathrm{a}_{13,4} = \mathrm{a}_{13,5} = \mathrm{a}_{13,6} = \mathrm{a}_{13,7} = \mathrm{a}_{13,8} = \mathrm{a}_{14,1} = \mathrm{a}_{14,2} = \mathrm{a}_{14,3} = \mathrm{a}_{14,4} \\ &= \mathrm{a}_{14,5} = \mathrm{a}_{14,6} = \mathrm{a}_{14,7} = \mathrm{a}_{14,8} = 0, \end{aligned} \tag{A1}$$

$$\begin{aligned} \mathrm{a}_{1,2} &= \mathrm{a}_{1,3} = \mathrm{a}_{1,4} = -\mathrm{a}_{4,6} = -\mathrm{a}_{4,7} = -\mathrm{a}_{4,8} = -\mathrm{a}_{8,10} = -\mathrm{a}_{8,11} = -\mathrm{a}_{8,12} = -\mathrm{a}_{14,13} \\ &= -\mathrm{a}_{14,14} = 1, \end{aligned} \tag{A2}$$

$$\mathrm{a}_{2,1} = -\mathrm{a}_{3,5} = -\mathrm{a}_{7,9} = \mathrm{a}_{13,13} = k, \tag{A3}$$

$$\mathrm{a}_{2,3} = -\mathrm{a}_{2,4} = m_1, \tag{A4}$$

$$\mathrm{a}_{3,1} = k \ \cosh(kd_1), \tag{A5}$$

$$a_{3,2} = k\ \sinh(kd_1), \tag{A6}$$

$$a_{3,3} = m_1 \exp(m_1 d_1), \tag{A7}$$

$$a_{3,4} = -m_1\ \exp(-m_1 d_1), \tag{A8}$$

$$a_{3,7} = -a_{3,8} = -m_2, \tag{A9}$$

$$a_{4,1} = \sinh(kd_1), \tag{A10}$$

$$a_{4,2} = \cosh(kd_1), \tag{A11}$$

$$a_{4,3} = \exp(m_1 d_1), \tag{A12}$$

$$a_{4,4} = \exp(-m_1 d_1), \tag{A13}$$

$$a_{5,1} = 2\mathrm{i}\rho_1\nu_1 k \sinh(kd_1) - \frac{E_{12}k^2}{\omega}\cosh(kd_1), \tag{A14}$$

$$a_{5,2} = 2\mathrm{i}\rho_1\nu_1 k \cosh(kd_1) - \frac{E_{12}k^2}{\omega}\sinh(kd_1), \tag{A15}$$

$$a_{5,3} = \left[\frac{\mathrm{i}\rho_1\nu_1}{k}\left(m_1^2 + k^2\right) - \frac{E_{12}km_1}{\omega}\right]\exp(m_1 d_1), \tag{A16}$$

$$a_{5,4} = \left[\frac{\mathrm{i}\rho_1\nu_1}{k}\left(m_1^2 + k^2\right) + \frac{E_{12}km_1}{\omega}\right]\exp(-m_1 d_1), \tag{A17}$$

$$a_{5,6} = -2\mathrm{i}\rho_2\nu_2 k, \tag{A18}$$

$$a_{5,7} = a_{5,8} = -\frac{\mathrm{i}\rho_2\nu_2}{k}\left(m_2^2 + k^2\right), \tag{A19}$$

$$a_{6,1} = \frac{\rho_1\nu_1}{k}\left(m_1^2 + k^2\right)\cosh(kd_1) + \mathrm{i}\left[\frac{(\rho_1 - \rho_2)g}{\omega} + \frac{T_{12}k^2}{\omega}\right]\sinh(kd_1), \tag{A20}$$

$$a_{6,2} = \frac{\rho_1\nu_1}{k}\left(m_1^2 + k^2\right)\sinh(kd_1) + \mathrm{i}\left[\frac{(\rho_1 - \rho_2)g}{\omega} + \frac{T_{12}k^2}{\omega}\right]\cosh(kd_1), \tag{A21}$$

$$a_{6,3} = \left[\frac{\mathrm{i}(\rho_1 - \rho_2)g}{\omega} + \frac{\mathrm{i}\ T_{12}k^2}{\omega} + 2\rho_1\nu_1 m_1\right]\exp(m_1 d_1), \tag{A22}$$

$$a_{6,4} = \left[\frac{\mathrm{i}(\rho_1 - \rho_2)g}{\omega} + \frac{\mathrm{i}\ T_{12}k^2}{\omega} - 2\rho_1\nu_1 m_1\right]\exp(-m_1 d_1), \tag{A23}$$

$$a_{6,5} = -\frac{\rho_2\nu_2}{k}\left(m_2^2 + k^2\right), \tag{A24}$$

$$-a_{6,7} = a_{6,8} = 2\rho_2\nu_2 m_2, \tag{A25}$$

$$a_{7,5} = k\cosh(kd_2), \tag{A26}$$

$$a_{7,6} = k\sinh(kd_2), \tag{A27}$$

$$a_{7,7} = m_2 \exp(m_2 d_2), \tag{A28}$$

$$\mathrm{a}_{7,8} = -m_2 \exp(-m_2 d_2), \tag{A29}$$

$$\mathrm{a}_{7,11} = -\mathrm{a}_{7,12} = -m_3, \tag{A30}$$

$$\mathrm{a}_{8,5} = \sinh(kd_2), \tag{A31}$$

$$\mathrm{a}_{8,6} = \cosh(kd_2), \tag{A32}$$

$$\mathrm{a}_{8,7} = \exp(m_2 d_2), \tag{A33}$$

$$\mathrm{a}_{8,8} = \exp(-m_2 d_2), \tag{A34}$$

$$\mathrm{a}_{9,5} = 2\mathrm{i}\rho_2 \nu_2 k \sinh(kd_2) - \frac{E_{23}k^2}{\omega} \cosh(kd_2), \tag{A35}$$

$$\mathrm{a}_{9,6} = 2\mathrm{i}\rho_2 \nu_2 k \cosh(kd_2) - \frac{E_{23}k^2}{\omega} \sinh(kd_2), \tag{A36}$$

$$\mathrm{a}_{9,7} = \left[\frac{\mathrm{i}\rho_2 \nu_2}{k}\left(m_2^2 + k^2\right) - \frac{E_{23}km_2}{\omega}\right] \exp(m_2 d_2), \tag{A37}$$

$$\mathrm{a}_{9,8} = \left[\frac{\mathrm{i}\rho_2 \nu_2}{k}\left(m_2^2 + k^2\right) + \frac{E_{23}km_2}{\omega}\right] \exp(-m_2 d_2), \tag{A38}$$

$$\mathrm{a}_{9,10} = -2\mathrm{i}\rho_3 \nu_3 k, \tag{A39}$$

$$\mathrm{a}_{9,11} = \mathrm{a}_{9,12} = -\frac{\mathrm{i}\rho_3 \nu_3}{k}\left(m_3^2 + k^2\right), \tag{A40}$$

$$\mathrm{a}_{10,5} = \frac{\rho_2 \nu_2}{k}\left(m_2^2 + k^2\right) \cosh(kd_2) + \mathrm{i}\left[\frac{(\rho_2 - \rho_3)g}{\omega} + \frac{T_{23}k^2}{\omega}\right] \sinh(kd_2), \tag{A41}$$

$$\mathrm{a}_{10,6} = \frac{\rho_2 \nu_2}{k}\left(m_2^2 + k^2\right) \sinh(kd_2) + \mathrm{i}\left[\frac{(\rho_2 - \rho_3)g}{\omega} + \frac{T_{23}k^2}{\omega}\right] \cosh(kd_2), \tag{A42}$$

$$\mathrm{a}_{10,7} = \left[\frac{\mathrm{i}\ (\rho_2 - \rho_3)g}{\omega} + 2\rho_2 \nu_2 m_2 + \frac{\mathrm{i}\ T_{23}k^2}{\omega}\right] \exp(m_2 d_2), \tag{A43}$$

$$\mathrm{a}_{10,8} = \left[\frac{\mathrm{i}\ (\rho_2 - \rho_3)g}{\omega} - 2\rho_2 \nu_2 m_2 + \frac{\mathrm{i}\ T_{23}k^2}{\omega}\right] \exp(-m_2 d_2), \tag{A44}$$

$$\mathrm{a}_{10,9} = -\frac{\rho_3 \nu_3}{k}\ \left(m_3^2 + k^2\right), \tag{A45}$$

$$\mathrm{a}_{10,11} = -\mathrm{a}_{10,12} = -2\rho_3 \nu_3 m_3, \tag{A46}$$

$$\mathrm{a}_{11,9} = 2\mathrm{i}\rho_3 \nu_3 k\ \ \sinh(kd_3) - \frac{E_{34}k^2}{\omega} \cosh(kd_3), \tag{A47}$$

$$\mathrm{a}_{11,10} = 2\mathrm{i}\rho_3 \nu_3 k\ \ \cosh(kd_3) - \frac{E_{34}k^2}{\omega} \sinh(kd_3), \tag{A48}$$

$$\mathrm{a}_{11,11} = \left[\frac{\mathrm{i}\rho_3 \nu_3}{k}\left(m_3^2 + k^2\right) - \frac{E_{34}km_3}{\omega}\right] \exp(m_3 d_3), \tag{A49}$$

$$\mathrm{a}_{11,12} = \left[\frac{\mathrm{i}\rho_3 \nu_3}{k}\left(m_3^2 + k^2\right) + \frac{E_{34}km_3}{\omega}\right] \exp(-m_3 d_3), \tag{A50}$$

$$\mathrm{a}_{11,13} = -2\mathrm{i}\rho_4\nu_4 k, \tag{A51}$$

$$\mathrm{a}_{11,14} = -\frac{\mathrm{i}\rho_4\nu_4}{k}\left(m_4^2 + k^2\right), \tag{A52}$$

$$\mathrm{a}_{12,9} = \frac{\rho_3\nu_3}{k}\left(m_3^2 + k^2\right)\cosh(kd_3) + \mathrm{i}\left[\frac{(\rho_3 - \rho_4)g}{\omega} + \frac{T_{34}k^2}{\omega}\right]\sinh(kd_3), \tag{A53}$$

$$\mathrm{a}_{12,10} = \frac{\rho_3\nu_3}{k}\left(m_3^2 + k^2\right)\sinh(kd_3) + \mathrm{i}\left[\frac{(\rho_3 - \rho_4)g}{\omega} + \frac{T_{34}k^2}{\omega}\right]\cosh(kd_3), \tag{A54}$$

$$\mathrm{a}_{12,11} = \left[\frac{\mathrm{i}\,(\rho_3 - \rho_4)g}{\omega} + 2\rho_3\nu_3 m_3 + \frac{\mathrm{i}\,T_{34}k^2}{\omega}\right]\exp(m_3 d_3), \tag{A55}$$

$$\mathrm{a}_{12,12} = \left[\frac{\mathrm{i}\,(\rho_3 - \rho_4)g}{\omega} - 2\rho_3\nu_3 m_3 + \frac{\mathrm{i}\,T_{34}k^2}{\omega}\right]\exp(-m_3 d_3), \tag{A56}$$

$$\mathrm{a}_{12,13} = \frac{\rho_4\nu_4}{k}\left(m_4^2 + k^2\right), \tag{A57}$$

$$\mathrm{a}_{12,14} = 2\rho_4\nu_4 m_4, \tag{A58}$$

$$\mathrm{a}_{13,9} = \mathrm{a}_{14,10} = k\ \cosh(kd_3), \tag{A59}$$

$$\mathrm{a}_{13,10} = \mathrm{a}_{14,9} = k\ \sinh(kd_3), \tag{A60}$$

$$\mathrm{a}_{13,11} = m_3\exp(m_3 d_3), \tag{A61}$$

$$\mathrm{a}_{13,12} = -m_3\exp(-m_3 d_3), \tag{A62}$$

$$\mathrm{a}_{13,14} = m_4, \tag{A63}$$

$$\mathrm{a}_{14,11} = \exp(m_3 d_3), \tag{A64}$$

$$\mathrm{a}_{14,12} = \exp(-m_3 d_3). \tag{A65}$$

[1] E. Abolfazli, J.-H. Liang, Y. Fan, Q. J. Chen, N. D. Walker, and J. Liu, Surface gravity waves and their role in ocean-atmosphere coupling in the Gulf of Mexico, J. Geophys. Res.: Oceans **125**, e2018JC014820 (2020).

[2] J. H. P. Studholme, M. Y. Markina, and S. K. Gulev, Role of surface gravity waves in aquaplanet ocean climates, J. Adv. Model. Earth Syst. **13**, e2020MS002202 (2021).

[3] S. E. Brumer, V. Garnier, J.-L. Redelsperger, M.-N. Bouin, F. Ardhuin, and M. Accensi, Impacts of surface gravity waves on a tidal front: A coupled model perspective, Ocean Modell. **154**, 101677 (2020).

[4] L. Wu, E. Sahlée, E. Nilsson, and A. Rutgersson, A review of surface swell waves and their role in air–sea interactions, Ocean Modell. **190**, 102397 (2024).

[5] J. E. Stopa, F. Ardhuin, R. Husson, H. Jiang, B. Chapron, and F. Collard, Swell dissipation from 10 years of Envisat advanced synthetic aperture radar in wave mode, Geophys. Res. Lett. **43**, 3423 (2016).

[6] D. M. Henderson and H. Segur, The role of dissipation in the evolution of ocean swell, J. Geophys. Res.: Oceans **118**, 5074 (2013).

[7] G. K. Rajan, A three-fluid model for the dissipation of interfacial capillary-gravity waves, Phys. Fluids **32**, 122121 (2020).

[8] C. R. Zaug and J. D. Carter, Dissipative models of swell propagation across the Pacific, Stud. Appl. Math. **147**, 1519 (2021).
[9] W. G. Van Dorn, Boundary dissipation of oscillatory waves, J. Fluid Mech. **24**, 769 (1966).
[10] D. Benielli and J. Sommeria, Excitation and breaking of internal gravity waves by parametric instability, J. Fluid Mech. **374**, 117 (1998).
[11] D. Henderson, G. K. Rajan, and H. Segur, Dissipation of narrow-banded surface water waves, in *Hamiltonian Partial Differential Equations and Applications*, edited by P. Guyenne, D. Nicholls, and C. Sulem, Fields Institute Communications, Vol. 75 (Springer, New York, 2015), pp. 163–183.
[12] I. Sergievskaya, S. Ermakov, T. Lazareva, and J. Guo, Damping of surface waves due to crude oil/oil emulsion films on water, Mar. Pollut. Bull. **146**, 206 (2019).
[13] R. A. Dalrymple and P. L. Liu, Waves over soft muds: A two-layer fluid model, J. Phys. Oceanogr. **8**, 1121 (1978).
[14] H. G. Gade, Effects of a nonrigid, impermeable bottom on plane surface waves in shallow water, J. Mar. Res. **16**, 61 (1958).
[15] J. P.-Y. Maa and A. J. Mehta, Soft mud response to water waves, J. Waterway Port Coastal Ocean Eng. **116**, 634 (1990).
[16] C.-O. Ng, Water waves over a muddy bed: A two-layer Stokes' boundary layer model, Coastal Eng. **40**, 221 (2000).
[17] P. L.-F. Liu and I.-C. Chan, A note on the effects of a thin visco-elastic mud layer on small amplitude water-wave propagation, Coastal Eng. **54**, 233 (2007).
[18] S. J. Williams and D.-S. Jeng, Viscous attenuation of interfacial waves over a porous seabed, J. Coastal Res. **SI 50**, 338 (2007).
[19] S. Elgar and B. Raubenheimer, Wave dissipation by muddy seafloors, Geophys. Res. Lett. **35**, 2008GL033245 (2008).
[20] M. Jain and A. J. Mehta, Role of basic rheological models in determination of wave attenuation over muddy seabeds, Cont. Shelf Res. **29**, 642 (2009).
[21] M. A. Aleebrahim and M. Jamali, Experimental investigation of instability of fluid mud layer under surface wave motion, Phys. Fluids **34**, 036602 (2022).
[22] H. Chou, J. Hunt, and M. Foda, Fluidization of marine mud by waves, Mar. Pollut. Bull. **23**, 75 (1991).
[23] Y. Li and A. Mehta, Fluid mud in the wave-dominated environment revisited, in *Coastal and Estuarine Fine Sediment Processes*, edited by W. H. McAnally and A. J. Mehta, Proceedings in Marine Science, Vol. 3 (Elsevier, The Netherlands, 2000), pp. 79–93.
[24] I. Safak and C. Sahin, Estimation of surface wave induced fluid mud thickness on the seafloor, Estuarine Coastal Shelf Sci. **267**, 107735 (2022).
[25] J. T. Wells, Dynamics of coastal fluid muds in low-, moderate-, and high-tide-range environments, Can. J. Fish. Aquat. Sci. **40**, s130 (1983).
[26] H. Macpherson, The attenuation of water waves over a non-rigid bed, J. Fluid Mech. **97**, 721 (1980).
[27] N. M. Frew and R. K. Nelson, Spatial mapping of sea surface microlayer surfactant concentration and composition, in *IEEE 1999 International Geoscience and Remote Sensing Symposium* (IEEE, Hamburg, Germany, 1999), Vol. 3, pp. 1472–1474.
[28] I. R. Jenkinson, L. Seuront, H. Ding, and F. Elias, Biological modification of mechanical properties of the sea surface microlayer, influencing waves, ripples, foam and air-sea fluxes, Elem. Sci. Anth. **6**, 26 (2018).
[29] B. Mithun Sundhar and G. K. Rajan, Characterizing ocean surface contamination: Composition, film thickness, and rheology, Mar. Pollut. Bull. **186**, 114287 (2023).
[30] S. Ermakov, O. Danilicheva, I. Kapustin, O. Shomina, I. Sergievskazya, A. Kupaev, and A. Molkov, Film slicks on the sea surface: Their dynamics and remote sensing, in *IGARSS 2020-2020 IEEE International Geoscience and Remote Sensing Symposium* (IEEE, Waikoloa, HI, USA, 2020), pp. 3545–3548.
[31] M. Gade, H. Hühnerfuss, and G. M. Korenowski, *Marine Surface Films: Chemical Characteristics, Influence on Air-Sea Interactions and Remote Sensing* (Springer, Berlin, 2006).

[32] A. D. Jenkins and S. J. Jacobs, Wave damping by a thin layer of viscous fluid, Phys. Fluids **9**, 1256 (1997).
[33] J. T. Davies and R. W. Vose, On the damping of capillary waves by surface films, Proc. R. Soc. London A **286**, 218 (1965).
[34] J. Aitken, On the effect of oil on a stormy sea, Proc. R. Soc. Edinburgh **12**, 56 (1884).
[35] B. Franklin, W. Brownrigg, and Farish, XLIV. Of the stilling of waves by means of oil. Extracted from sundry letters between Benjamin Franklin, LL. D. F. R. S. William Brownrigg, M. D. F. R. S. and the Reverend Mr. Farish, Philos. Trans. R. Soc. **64**, 445 (1774).
[36] D. Lohse, Surfactants on troubled waters, J. Fluid Mech. **976**, F1 (2023).
[37] B. D. Dore, Some effects of the air-water interface on gravity waves, Geophys. Astrophys. Fluid Dyn. **10**, 215 (1978).
[38] W. Alpers and H. Hühnerfuss, The damping of ocean waves by surface films: A new look at an old problem, J. Geophys. Res.: Oceans **94**, 6251 (1989).
[39] V. Žutić, B. Ćosović, E. Marčenko, N. Bihari, and F. Kršinić, Surfactant production by marine phytoplankton, Mar. Chem. **10**, 505 (1981).
[40] E. J. Bock and N. M. Frew, Static and dynamic response of natural multicomponent oceanic surface films to compression and dilation: Laboratory and field observations, J. Geophys. Res.: Oceans **98**, 14599 (1993).
[41] J. T. Mass, Dynamic properties of seawater surfactants, M.S. Thesis, Massachusetts Institute of Technology, 1996.
[42] R. Dorrestein, General linearized theory of the effect of surface films on water ripples, Proc. K. Ned. Akad. Wet. B **54**, 260 (1951).
[43] J. Lucassen, Longitudinal capillary waves. Part 1. Theory, Trans. Faraday Soc. **64**, 2221 (1968).
[44] E. H. Lucassen-Reynders and J. Lucassen, Properties of capillary waves, Adv. Colloid Interface Sci. **2**, 347 (1970).
[45] J. Lucassen, Effect of surface-active material on the damping of gravity waves: A reappraisal, J. Colloid Interface Sci. **85**, 52 (1982).
[46] H. Segur, D. Henderson, J. Carter, J. Hammack, C.-M. Li, D. Pheiff, and K. Socha, Stabilizing the Benjamin-Feir instability, J. Fluid Mech. **539**, 229 (2005).
[47] S. J. Brown, M. S. Triantafyllou, and D. K. P. Yue, Complex analysis of resonance conditions for coupled capillary and dilational waves, Proc. R. Soc. London, Ser. A **458**, 1167 (2002).
[48] S. A. Ermakov, Resonance damping of gravity-capillary waves on the water surface covered with a surface active film, Izv. Atmos. Oceanic Phys. **39**, 624 (2003).
[49] S. Ermakov, I. Sergievskaya, and L. Gushchin, Damping of gravity-capillary waves in the presence of oil slicks according to data from laboratory and numerical experiments, Izv. Atmos. Oceanic Phys. **48**, 565 (2012).
[50] G. K. Rajan, Dissipation of interfacial Marangoni waves and their resonance with capillary-gravity waves, Int. J. Eng. Sci. **154**, 103340 (2020).
[51] S. A. Ermakov and G. E. Khazanov, Resonance damping of gravity–capillary waves on water covered with a visco-elastic film of finite thickness: A reappraisal, Phys. Fluids **34**, 092107 (2022).
[52] H. Manikantan and T. M. Squires, Surfactant dynamics: Hidden variables controlling fluid flows, J. Fluid Mech. **892**, P1 (2020).
[53] F. Ardhuin, B. Chapron, and F. Collard, Observation of swell dissipation across oceans, Geophys. Res. Lett. **36**, 2008GL037030 (2009).
[54] F. Collard, F. Ardhuin, and B. Chapron, Monitoring and analysis of ocean swell fields from space: New methods for routine observations, J. Geophys. Res.: Oceans **114**, 2008JC005215 (2009).
[55] H. Jiang, J. E. Stopa, H. Wang, R. Husson, A. Mouche, B. Chapron, and G. Chen, Tracking the attenuation and nonbreaking dissipation of swells using altimeters, J. Geophys. Res.: Oceans **121**, 1446 (2016).
[56] F. E. Snodgrass, G. W. Groves, K. F. Hasselmann, G. R. Miller, W. H. Munk, and W. H. Powers, Propagation of ocean swell across the Pacific, Philos. Trans. R. Soc. London, Ser. A **259**, 431 (1966).

[57] N. E. Canney and J. D. Carter, Stability of plane waves on deep water with dissipation, Math. Comput. Simul. **74**, 159 (2007).
[58] J. D. Carter and C. C. Contreras, Stability of plane-wave solutions of a dissipative generalization of the nonlinear Schrödinger equation, Physica D **237**, 3292 (2008).
[59] A. D. Craik, George Gabriel Stokes on water wave theory, Annu. Rev. Fluid Mech. **37**, 23 (2005).
[60] G. G. Stokes, On the theory of oscillatory waves, in *Mathematical and Physical Papers* (Cambridge University Press, Cambridge, 2009), Vol. 1, pp. 197–229.
[61] H. Lamb, *Hydrodynamics*, 6th ed. (Cambridge University Press, Cambridge, 1932).
[62] W. J. Harrison, The influence of viscosity on the oscillations of superposed fluids, Proc. London Math. Soc. **s2-6**, 396 (1908).
[63] V. G. Levich, *Physicochemical Hydrodynamics: (by) Veniamin G. Levich, Transl. by Scripta Technica, Inc.*, Prentice-Hall International Series in the Physical and Chemical Engineering Sciences (Prentice-Hall, New York, 1962).
[64] L. M. Hocking, The damping of capillary-gravity waves at a rigid boundary, J. Fluid Mech. **179**, 253 (1987).
[65] J. Kamphuis, Attenuation of gravity waves by bottom friction, Coastal Eng. **2**, 111 (1978).
[66] J. Hunt, The viscous damping of gravity waves in shallow water, Houille Blanche **50**, 685 (1964).
[67] C. C. Mei and L. F. Liu, The damping of surface gravity waves in a bounded liquid, J. Fluid Mech. **59**, 239 (1973).
[68] K. M. Case and W. C. Parkinson, Damping of surface waves in an incompressible liquid, J. Fluid Mech. **2**, 172 (1957).
[69] G. H. Keulegan, Energy dissipation in standing waves in rectangular basins, J. Fluid Mech. **6**, 33 (1959).
[70] T. B. Benjamin and F. Ursell, The stability of the plane free surface of a liquid in vertical periodic motion, Proc. R. Soc. London A **225**, 505 (1954).
[71] J. Lucassen and E. Lucassen-Reynders, Wave damping and gibbs elasticity for nonideal surface behavior, J. Colloid Interface Sci. **25**, 496 (1967).
[72] K. Dysthe and Y. Rabin, Damping of short waves by insoluble surface films, Technical report C-11-86, U. S. Office of Naval Research, London (1986).
[73] V. G. Levich, Damping of waves by surface-active substances. I, Acta Physicochim. URSS **14**, 307 (1941).
[74] P. P. Lombardini, F. Piazzese, and R. Cini, The marangoni wave in ripples on an air-water interface covered by a spreading film, Nuovo Cimento C **5**, 256 (1982).
[75] H. Hühnerfuss, W. Alpers, W. D. Garrett, P. A. Lange, and S. Stolte, Attenuation of capillary and gravity waves at sea by monomolecular organic surface films, J. Geophys. Res. **88**, 9809 (1983).
[76] P. L. Ghia and P. Trivero, On the vibration modes of the air-water interface in the presence of surface films, Nuovo Cimento C **11**, 450 (1988).
[77] G. K. Batchelor, *An Introduction to Fluid Dynamics* (Cambridge University Press, 1967).
[78] B. Fiscella, P. P. Lombardini, P. Trivero, and R. Cini, Ripple damping on water surface covered by a spreading film: Theory and experiment, Nuovo Cimento C **8**, 491 (1985).
[79] M. P. Tulin, On the transport of energy in water waves, J. Eng. Math. **58**, 339 (2007).
[80] B. D. Dore, Oscillatory response of a monomolecular slick to progressive waves, Arch. Meteorol. Geophys. Bioklimatol., Ser. A **31**, 385 (1982).
[81] A. Shmidt, Damping of capillary-gravitational waves in a viscous fluid of finite depth by surfactants, J. Appl. Math. Mech. **30**, 901 (1966).
[82] M. Van Den Tempel and R. P. Van De Riet, Damping of waves by surface-active materials, J. Chem. Phys. **42**, 2769 (1965).
[83] R. Cini, P. P. Lombardini, and H. Hühnerfuss, Remote sensing of marine slicks utilizing their influence on wave spectra, Int. J. Remote Sens. **4**, 101 (1983).
[84] J. Lucassen and M. V. D. Tempel, Longitudinal waves on visco-elastic surfaces, J. Colloid Interface Sci. **41**, 491 (1972).
[85] J. W. Miles, Surface-wave damping in closed basins, Proc. R. Soc. London A **297**, 459 (1967).
[86] F. C. Goodrich, The mathematical theory of capillarity. II, Proc. R. Soc. London A **260**, 490 (1961).

[87] D. Dimitrov, I. Panaiotov, P. Richmond, and L. Ter-Minassian-Saraga, Dynamics of insoluble monolayers: I. dilatational or elastic modulus, friction coefficient, and Marangoni effect for dipalmitoyl lecithin monolayers, J. Colloid Interface Sci. **65**, 483 (1978).

[88] I. Sergievskaya and S. Ermakov, Damping of gravity–capillary waves on water surface covered with a visco-elastic film of finite thickness, Izv. Atmos. Oceanic Phys. **53**, 650 (2017).

[89] I. Sergievskaya and S. Ermakov, A phenomenological model of wave damping due to oil films, in *Remote Sensing of the Ocean, Sea Ice, Coastal Waters, and Large Water Regions 2019*, edited by C. R. Bostater, Jr., X. Neyt, and F. Viallefont-Robinet (SPIE, International Society for Optics and Photonics, Philadelphia, 2019), Vol. 11150, pp. 153–158.

[90] D. M. Henderson and J. W. Miles, Surface-wave damping in a circular cylinder with a fixed contact line, J. Fluid Mech. **275**, 285 (1994).

[91] L. A. Gushchin and S. A. Ermakov, Laboratory study of surfactant redistribution in the flow field induced by surface waves, Izv. Atmos. Oceanic Phys. **40**, 244 (2003).

[92] S. A. Ermakov and S. V. Kijashko, Laboratory study of the damping of parametric ripples due to surfactant films, in *Marine Surface Films*, edited by M. Gade, H. Hühnerfuss, and G. M. Korenowski (Springer, Berlin, Heidelberg, 2006), pp. 113–128.

[93] R. I. Slavchov, B. Peychev, and A. S. Ismail, Characterization of capillary waves: A review and a new optical method, Phys. Fluids **33**, 101303 (2021).

[94] D. M. Henderson, Effects of surfactants on Faraday-wave dynamics, J. Fluid Mech. **365**, 89 (1998).

[95] H. Hühnerfuss, P. Lange, and W. Walter, Wave damping by monomolecular surface films and their chemical structure. Part I: Variation of the hydrophobic part of carboxylic acid esters, J. Mar. Res. **40**, 209 (1982).

[96] H. Hühnerfuss, P. A. Lange, and W. Walter, Wave damping by monomolecular surface films and their chemical structure. Part II: Variation of the hydrophilic part of the film molecules including natural substances, J. Mar. Res. **42**, 737 (1984).

[97] H. Hühnerfuss, P. A. Lange, and W. Walter, Relaxation effects in monolayers and their contribution to water wave damping: I. Wave-induced phase shifts, J. Colloid Interface Sci. **108**, 430 (1985).

[98] H. Hühnerfuss, P. A. Lange, and W. Walter, Relaxation effects in monolayers and their contribution to water wave damping: II. The Marangoni phenomenon and gravity wave attenuation, J. Colloid Interface Sci. **108**, 442 (1985).

[99] G. Sutherland, T. Halsne, J. Rabault, and A. Jensen, The attenuation of monochromatic surface waves due to the presence of an inextensible cover, Wave Motion **68**, 88 (2017).

[100] A. Nägeli and F. Schanz, The influence of extracellular algal products on the surface tension of water, Int. Rev. Gesamten Hydrobiol. Hydrogr. **76**, 89 (1991).

[101] Q. Wang, A. Feder, and E. Mazur, Capillary wave damping in heterogeneous monolayers, J. Phys. Chem. **98**, 12720 (1994).

[102] J. Lucassen and R. S. Hansen, Damping of waves on monolayer-covered surfaces: I. Systems with negligible surface dilational viscosity, J. Colloid Interface Sci. **22**, 32 (1966).

[103] R. Cini, P. P. Lombardini, C. Manfredi, and E. Cini, Ripples damping due to monomolecular films, J. Colloid Interface Sci. **119**, 74 (1987).

[104] J. Lucassen and M. V. D. Tempel, Dynamic measurements of dilational properties of a liquid interface, Chem. Eng. Sci. **27**, 1283 (1972).

[105] J. T. Mass and J. H. Milgram, Dynamic behavior of natural sea surfactant films, J. Geophys. Res.: Oceans **103**, 15695 (1998).

[106] A. Z. Mazurek and S. J. Pogorzelski, Elastic properties of natural sea surface films incorporated with solid dust particles: Model Baltic sea studies, Int. J. Oceanogr. **2012**, 638240 (2012).

[107] B. Noskov and T. Zubkova, Dilational surface properties of insoluble monolayers, J. Colloid Interface Sci. **170**, 1 (1995).

[108] F. De Voeght and P. Joos, Damping of a disturbance on a liquid surface, J. Colloid Interface Sci. **98**, 20 (1984).

[109] R. S. Hansen and J. Ahmad, Waves at interfaces, in *Progress in Surface and Membrane Science*, edited by J. F. Danielli, M. D. Rosenberg, and D. A. Cadenhead (Academic Press, USA, 1971), Vol. 4, pp. 1–56.

[110] G. K. Rajan and D. M. Henderson, Linear waves at a surfactant-contaminated interface separating two fluids: Dispersion and dissipation of capillary-gravity waves, Phys. Fluids **30**, 072104 (2018).

[111] Ø. Saetra, Effects of surface film on the linear stability of an air–sea interface, J. Fluid Mech. **357**, 59 (1998).

[112] K. Mahshid, S. Ghader, S. H. Shamsnia, and S. A. Haghshenas, An analytical solution to wave dissipation induced by interacting waves and currents with muddy deposits, Ocean Dyn. **72**, 715 (2022).

[113] S. H. Shamsnia, S. A. Haghshenas, S. Ghader, and K. Mahshid, An analytical model for mass transport calculations in a viscous muddy layer, Appl. Ocean Res. **115**, 102816 (2021).

[114] S. H. Shamsnia and D. Dutykh, An analytical study on wave-current-mud interaction, Water **12**, 2899 (2020).

[115] Y.-Z. Xia and K.-Q. Zhu, A study of wave attenuation over a Maxwell model of a muddy bottom, Wave Motion **47**, 601 (2010).

[116] E.-I. Garnier, Z. Huang, and C. C. Mei, Nonlinear long waves over a muddy beach, J. Fluid Mech. **718**, 371 (2013).

[117] I.-C. Chan, Theoretical model for nonlinear long waves over a thin viscoelastic muddy seabed, Mathematics **10**, 2715 (2022).

[118] D. J. Robillard, A. J. Mehta, and I. Safak, Comments on wave-induced behavior of a coastal mud, Coastal Eng. **186**, 104400 (2023).

[119] W.-Y. Hsu, H.-H. Hwung, R.-Y. Yang, and C.-M. Liu, Interfacial wave motion caused by wave-mud interaction, J. Visualization **15**, 215 (2012).

[120] W. Hsu, H. Hwung, T. Hsu, A. Torres-Freyermuth, and R. Yang, An experimental and numerical investigation on wave-mud interactions, J. Geophys. Res.: Oceans **118**, 1126 (2013).

[121] H. Mac Pherson and P. Kurup, Wave damping at the Kerala mudbanks, Indian J. Marine Sci. **10**, 154 (1981).

[122] Y. Nouri, Experimental study of water wave interactions with a layer of mud, Ph.D. thesis, The Johns Hopkins University, 2013.

[123] N. Almashan and R. A. Dalrymple, Damping of waves propagating over a muddy bottom in deep water: Experiment and theory, Coastal Eng. **105**, 36 (2015).

[124] S. A. Haghshenas and M. Soltanpour, An analysis of wave dissipation at the Hendijan mud coast, the Persian Gulf, Ocean Dyn. **61**, 217 (2011).

[125] A. Quesada, E. Bautista, and F. Méndez, Damping coefficient by long waves—Viscoelastic mud–current interaction, Phys. Fluids **34**, 093111 (2022).

[126] S. H. Shamsnia, M. Soltanpour, M. Bavandpour, and C. Gualtieri, A study of wave dissipation rate and particles velocity in muddy beds, Geosciences **9**, 212 (2019).

[127] Y.-Z. Xia, The attenuation of shallow-water waves over seabed mud of a stratified viscoelastic model, Coastal Eng. J. **56**, 1450021 (2014).

[128] L. Huang and Q. Chen, Spectral collocation model for solitary wave attenuation and mass transport over viscous mud, J. Eng. Mech. **135**, 881 (2009).

[129] K. Newyear and S. Martin, A comparison of theory and laboratory measurements of wave propagation and attenuation in grease ice, J. Geophys. Res.: Oceans **102**, 25091 (1997).

[130] R. Wang and H. H. Shen, Experimental study on surface wave propagating through a grease–pancake ice mixture, Cold Reg. Sci. Technol. **61**, 90 (2010).

[131] D. K. Sree, A. W.-K. Law, and H. H. Shen, An experimental study on the interactions between surface waves and floating viscoelastic covers, Wave Motion **70**, 195 (2017), Recent Advances on Wave Motion in Fluids and Solids.

[132] D. K. Sree, A. W.-K. Law, and H. H. Shen, An experimental study on gravity waves through a floating viscoelastic cover, Cold Reg. Sci. Technol. **155**, 289 (2018).

[133] D. K. Sree, A. W.-K. Law, and H. H. Shen, An experimental study of gravity waves through segmented floating viscoelastic covers, Appl. Ocean Res. **101**, 102233 (2020).

[134] G. K. Rajan, Damping rate measurements and predictions for gravity waves in an air–oil–water system, Phys. Fluids **34**, 022113 (2022).
[135] J. B. Keller, Gravity waves on ice-covered water, J. Geophys. Res.: Oceans **103**, 7663 (1998).
[136] G. De Carolis and D. Desiderio, Dispersion and attenuation of gravity waves in ice: A two-layer viscous fluid model with experimental data validation, Phys. Lett. A **305**, 399 (2002).
[137] R. Wang and H. H. Shen, Gravity waves propagating into an ice-covered ocean: A viscoelastic model, J. Geophys. Res.: Oceans **115**, C06024 (2010).
[138] H. Chen, R. P. Gilbert, and P. Guyenne, Dispersion and attenuation in a porous viscoelastic model for gravity waves on an ice-covered ocean, Eur. J. Mech. B. Fluids **78**, 88 (2019).
[139] X. Zhao and H. H. Shen, Three-layer viscoelastic model with eddy viscosity effect for flexural-gravity wave propagation through ice cover, Ocean Modell. **131**, 15 (2018).
[140] M. G. Velarde and X.-L. Chu, *The Harmonic Oscillator Description of Longitudinal (Marangoni-Lucassen) Waves at Liquid Interfaces* (Springer US, Boston, 1988), pp. 183–187.
[141] M. G. Velarde and X.-L. Chu, The harmonic oscillator approach to sustained gravity-capillary (laplace) waves at liquid interfaces, Phys. Lett. A **131**, 430 (1988).
[142] X.-L. Chu and M. G. Velarde, Transverse and longitudinal waves induced and sustained by surfactant gradients at liquid-liquid interfaces, J. Colloid Interface Sci. **131**, 471 (1989).
[143] J. D. Barter, Surface strain modulation of insoluble surface film properties, Phys. Fluids **6**, 2606 (1994).
[144] S. Berg, Marangoni-driven spreading along liquid-liquid interfaces, Phys. Fluids **21**, 032105 (2009).
[145] Y. Hu, X. Guo, X. Lu, Y. Liu, R. A. Dalrymple, and L. Shen, Idealized numerical simulation of breaking water wave propagating over a viscous mud layer, Phys. Fluids **24**, 112104 (2012).
[146] B.-Q. Deng, Y. Hu, X. Guo, R. A. Dalrymple, and L. Shen, Numerical study on the dissipation of water waves over a viscous fluid-mud layer, Comput. Fluids **158**, 107 (2017).
[147] C. D. Troy and J. R. Koseff, The viscous decay of progressive interfacial waves, Phys. Fluids **18**, 026602 (2006).
[148] N. J. Laxague, C. J. Zappa, S. Soumya, and O. Wurl, The suppression of ocean waves by biogenic slicks, J. R. Soc. Interface **21**, 20240385 (2024).
[149] G. K. Rajan, Solutions of a comprehensive dispersion relation for waves at the elastic interface of two viscous fluids, Eur. J. Mech. B Fluids **89**, 241 (2021).
[150] L. Debnath, *Nonlinear Water Waves* (Academic Press, Boston, 1994).
[151] B. R. Sutherland, *Internal Gravity Waves* (Cambridge University Press, Cambridge, UK, 2010).
[152] L. Shay, Upper ocean structure: Responses to strong atmospheric forcing events, in *Encyclopedia of Ocean Sciences*, 2nd ed., edited by J. H. Steele (Academic Press, Oxford, 2009), pp. 192–210.
[153] H. G. Gade, Effects of a nonrigid, impermeable bottom on plane surface waves in shallow water, Ph.D. thesis, Texas A&M University, 1957.
[154] F. Jiang, Bottom mud transport due to water waves, Ph.D. thesis, University of Florida, 1993.
[155] B. Xu and P. Guyenne, Assessment of a porous viscoelastic model for wave attenuation in ice-covered seas, Appl. Ocean Res. **122**, 103122 (2022).